ELSEVIER

Contents lists available at ScienceDirect

# Composites Part B

journal homepage: www.elsevier.com/locate/compositesb



# Mechanical behavior of MXene-Polymer layered nanocomposite using computational finite element analysis

Anamika Prasad <sup>a,b,\*</sup>, Jason Hasse <sup>c</sup>, Timothy Steimle <sup>d</sup>, Dhriti Nepal <sup>e</sup>, Geoffrey J. Frank <sup>e,f</sup>, Vikas Varshney <sup>e,\*\*</sup>

- <sup>a</sup> Department of Biomedical Engineering, Florida International University, Miami, FL, USA
- b Department of Mechanical and Materials Engineering, Florida International University, Miami, FL, USA
- <sup>c</sup> Department of Mathematics and Statistics, South Dakota State University, Brookings, SD, USA
- <sup>d</sup> Department of Mechanical Engineering, Wright State University, Dayton, OH, USA
- e Materials and Manufacturing Directorate, Air Force Research Laboratory, Wright-Patterson Air Force Base, Dayton, OH, USA
- f University of Dayton Research Institute, Dayton, OH, USA

#### ARTICLE INFO

Handling Editor: Dr Uday Vaidya

Keywords: MXene Bioinspired Nanocomposite FEA Nacre

# ABSTRACT

The structural integrity of MXene and MXene-based materials is important across applications from sensors to energy storage. While MXene processing has received significant attention, its structural integrity for real-world applications remains challenging due to its flake-like structure. Here the mechanical response of layered MXenepolymer nanocomposites (MPC) with high MXene concentration (>70 %) and bioinspired nacre-like brick-andmortar architecture is investigated to offer insights for MPC design and processing. An automated finite element analysis (FEA) framework is developed to analyze MPC models with randomized geometries and multiple combinations of the parameter space. Specifically, the influence of concentration, aspect ratio (AR), flake thickness, flake distribution, and interfacial strength is investigated. The results reveal property trends such as increasing elastic modulus, strength, and toughness with increasing cohesive strength and concentration for lower AR (=40, 60) but a decreasing trend at higher AR of 75. Local structural features like flake distribution, overlapping MXene lengths, and interconnected polymers in adjacent layers was found a critical determinant of performance. For example, stronger cohesive interaction showed 6X high toughness (291  $\pm$  226  $KJ/m^3$ ) compared to weaker case (50  $\pm$  24  $KJ/m^3$ ), but the large scatter highlighted the impact of microstructural features. The results are compared and validated with theoretical, computational, and experimental work. The findings provide valuable guidance for optimizing MPC design and their processing. Finally, the automation of the framework allows the design to be extended beyond the current system and chosen material combinations.

# 1. Introduction

MXenes, a versatile two-dimensional (2D) material can simultaneously combine the high conductivity of metals in a thin low-density form factor with excellent mechanical stiffness. The unique multifunctionality of MXene is attributed to its formulation ( $M_{n+1}X_nT_x$  where M = early transition metals, X = carbon or nitrogen, and T = functional surface terminations) that allows it to have greater adaptability through elemental permutations and combinations. Hence MXene-based materials are desirable alternatives for various applications from energy storage, body armor, sensing, and bone reconstruction [1–7]. However,

while significant research has focused on processing resulting in a large family of MXenes [2,6,8], its flake-like form factor remains challenging in maintaining structural integrity across applications [9]. These characteristics have required a move towards MXene-polymer composites (MPC) to improve structural integrity.

MPC processing often leads to a layered design due to the inherent 2D architecture of MXenes. Layered MXene-based structures have been synthesized across several applications, such as supercapacitance, energy storage, wastewater treatment, air filtration, gas separators, body armors, and wearable electronics [10–13]. While the desired structural traits and optimal polymer concentration in layered MPC vary across

E-mail addresses: anprasad@fiu.edu (A. Prasad), vikas.varshney.2@us.af.mil (V. Varshney).

https://doi.org/10.1016/j.compositesb.2024.111689

<sup>\*</sup> Corresponding author. Department of Biomedical Engineering, Florida International University, Miami, FL, USA.

<sup>\*\*</sup> Corresponding author.

these applications, one of the common traits is the need to maintain high MXene concentration to not negatively impact its multifunctional traits (i.e., high conductivity and large surface area). These in turn require optimized structural design to carefully balance the need for structural stability with its other multifunctional demands across applications.

Highly mineralized layered composites such as nacre offer effective design templates for layered MPC [14–21]. They consist of highly mineralized tablets (>90 %) organized in a brick-mortar design with the mortar being the polymer interphase materials binding the layers and providing additional functionality of toughness and plasticity to the structure [14,22–28]. The geometrical parameters for individual tablets (size, thickness, and AR), the volume concentration of minerals and organics, and the interface interactions have all been carefully evolved over millennia for multifunctionality of stiffness and toughness together with other traits such as iridescent and saltwater resistance [29,30]. Hence, this well-studied natural system is an excellent model to inspire design traits for MPC.

The current work aims to investigate the mechanics of layered MPC with nacre-like bioinspired features using a FEA framework. While molecular dynamics (MD) simulations can investigate atomic-scale interactions between individual MXene sheets and polymer-MXene interfaces, it is limited due to size when it comes to capturing the response of larger systems such as micron-sized MPC geometries (for example, MXene composites with thin film form involving several MXene sheets). Continuum mechanics-based FEA can address the size limitations of atomistic simulations to model realistic geometries. Previous studies on biological [31–34] and engineered [35–38] nanocomposite have demonstrated the applicability of FEA to the nanoscale. Recent works have also applied FEA for studying pristine MXene sheets or low volume fraction MPC (maximum was 40 % in one study but typically below 1 %) [35,39–44].

Building on the past application of FEA to nanostructure and MXene, the current work extends the capability to investigate the mechanics of high-concentration (>70 %) layered MPC. The essential features of the work include (1) geometry and parameter space selection from bioinspired design, (2) automation for streamlining model creation and post-processing for large-scale parameter integration, and (3) insights into deformation and failure mechanisms to guide processing. The geometry and model automation were achieved by integrating Python script within the FEA framework using ABAQUS (Dassault Systemes, USA). The additional automation toolkit was developed in R Studio (RStudio, USA). The framework was applied to large permutations of the parameter space to create insights into the deformation mechanics and

failure of layered MPC.

#### 2. Materials and method

The model generation and FEA were performed using Abaqus (Dassault System, USA) on a high-performance cluster (HPC). Python scripting capability interfacing with ABAQUS was used to automate several aspects of the analysis and post-processing, as shown in the process framework of Fig. 1. These included the automation of model geometry and result data extraction for post-processing. The plots were autogenerated using coding in R Studio.

### 2.1. Model geometry

Geometrical parameters inspired by highly mineralized 2D composites was used to design the layered MPC. Specifically, nacre has a mineral concentration close to 95 %, and its structure is arranged in a brick-and-mortar form. The "bricks" are mineralized polygonal tablets with diameters of 5–20  $\mu m$  and thickness of 0.3–0.9  $\mu m$ , leading to AR of 20-100 [23,45-47]. Tablets are joined together with a thin layer of organic interphase "mortar," which is 20-50 nm [22,48]. Multiple tables are stacked together to form nacre sheets of 300-500  $\mu m$  depth. Other similar brick-and-mortar composites include the exoskeleton of windowpane oysters, which has diamond-shaped tablets of AR 500. The AR is critical for the toughness of nacreous material, with a theoretically derived critical AR of 25 leading to an optimum combination of strength and toughness, with higher values leading to higher strength at the cost of toughness [49,50]. The MPC film structure was inspired by the above-described brick-mortar architecture of the nacre, with the stiff MXene flake considered bricks and the interspersed polymer equivalent to the mortar of the nacreous sheet. While the flake thickness was guided by MXene atomic layering, the AR and flake concentration, which have a critical influence on mechanical response, were selected to match that of the nacre.

Fig. 2a shows the overall schematic of the chosen MPC with geometry parameters listed in the table (Fig. 2b). The constants of the model geometry were flake thickness (fT), total film length (L), and total number of layers (n). While the value of fT of 2.5 nm was guided by the atomic thickness reported for three-layered MXene [33], the flake AR (fAR) was taken as 40, 60, and 75, keeping with the range for nacre. In the MXene context, the AR of monolayer pristine MXene flakes varies from 500 to 1000 depending on processing parameters [51–54], with ultra-large but fragile flakes also reported [55]. In practical applications,

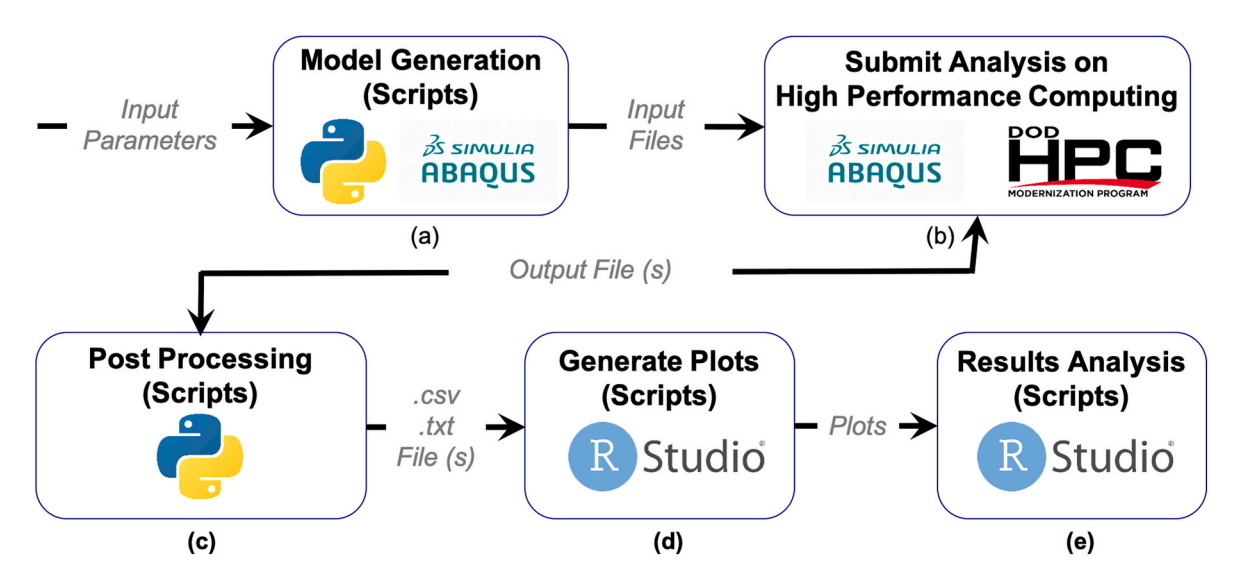


Fig. 1. Schematic framework for model generation, analysis, and post-processing. showing Python and R scripts integrated for the automation of simulation tasks, such as input file generation, post-processing files, plot generation, and results analysis.

Parameters	Range of Values
Flake Thickness (fT)	2.5 nm
No of flake layers (n)	12
Film thickness (D)	= n*fT = 30  nm
Flake Aspect Ratio (fAR)	40, 60, 75
Flake concentration ( $fC$ )	70% to 90%

**Fig. 2.** (a) Representative schematic of a geometry used for FEA analysis and (b) summary of model geometry parameters and ranges investigated in this study. The brick-and-mortar organization and the choice of geometrical parameters such as *fAR* were inspired by the nacre design.

however, the AR of MXene can be significantly reduced from its pristine single-layered form due to the fragility of flakes and processing challenges, resulting in smaller AR of 17–100 as reported in several cases [40,56,57], which are within the values used here. Furthermore, computationally, it becomes expensive to model micron-size flakes (AR > 500) while bringing significant stochastically in the modeling system. Hence, the chosen AR matches experimental data and provides computational efficiency in investigating model stochastic nature on the mechanical response.

The film length L of 750 nm was taken to accommodate more than three flakes for the range of AR selected. The number of layers *n* was 12, leading to a film thickness (D) of 30 nm. The adjacent flake layers were assumed to be directly in contact with zero 'effective' thickness in between. The contact response was modeled using cohesive interactions, as described later. As in the natural mineralized system, the mineral phase represented by stiff MXene was the dominant material, with targeted flake concentration (fC) values between 70 % and 90 %. Other reasons for choosing high concentrations of MXenes are twofold. First, often MPC are used for their multifunctionality that require film to be conductive (electrical percolation) as well as mechanically stable (binding with the polymer). Towards that, higher concentration of MXenes is desired to maintain electrical conductivity closer to that of MXene. Second, the simulations allows us to explore higher concentration regime of MPC which are not only practically relevant but also extends all prior studies which have been performed on much lower MXene concentrations.

As described in the supplemental information (SI) and Fig. S1, an automation process was used for model geometry creation. Since the automation process achieved randomness in flake-polymer distribution using an exponential distribution of polymer gaps, each model possessed unique geometry even with the same starting parameters (see SI-Fig. S2). Furthermore, since flakes were cut off and readjusted to fit within the designated box, the flake concentration achieved differed slightly ( $<\pm$  5 %) from the targeted value, resulting in a distribution of concentrations around the target (SI, Fig. S3). Hence, simulations were grouped in four-volume concentration blocks between 75 % and 95 %. Half of these geometries created were assigned strong contact interactions, while the other half were assigned weak interactions.

### 2.2. Materials

### 2.2.1. Polymer matrix

Polyvinyl alcohol (PVA) is chosen as the interphase material for the study. Multiple other polymers, including sodium alginate (SA) and cellulose, have been used as interphases in layered MPC films [8,58–61] and can be alternatively used. The use of PVA has several advantages, including water solubility for easy dispersibility, improved thermal stability, and biodegradability [62,63]. Specific to the MPC context, PVA hydrophilicity and the presence of hydroxyl groups make it have a good compatibility with MXene, making it an overall attractive choice for MPC design for an extensive range of applications [64–67]. Furthermore, the use of PVA in earlier simulations on MPC [39,40] can allow for a direct comparison of predictions.

An isotropic elastoplastic model with progressive damage and failure was used to capture the PVA response, with model parameters extracted to fit the experimental stress-strain data [61]. The material model is marked by distinct zones, namely linear elastic response defined by Young's modulus E=0.91 GPa, plastic response post-yield strength  $\sigma_y$  of 31.5 MPa, damage initiation defined using maximum equivalent fracture strain  $\varepsilon_f^{max}$  of 0.05, and damage evolution defined by the fracture energy  $G_f$  here taken as 0.

#### 2.2.2. MXene flake

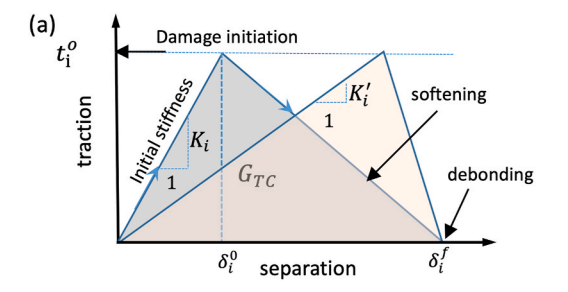
The material properties for flakes were based on literature data of pristine MXene flakes from experiments and MD simulations. Experimental investigation via nanoindentation on single and bilayer  $Ti_3C_2T_x$  showed a modulus of  $333\pm30$  GPa [68]. MD-based tensile test simulation on titanium carbide ( $Ti_nC_{n-1}$ , n=2,3,4) showed anisotropy and nonlinearity, with Young's modulus reported between 482 and 650 GPa [69–71]. MD simulation of nanoindentation also showed a higher modulus between 466 and 983 GPa for  $Ti_3C_2O_2$  and  $Ti_3CO$  [72]. However, the same study also demonstrated the role of a small % of vacancy defect in reducing the modulus to 386 GPa, mirroring closer to experimental data.

The response of MXene can also be better captured by using elastoplastic with a progressive damage model, as for PVA. However, since the stiffness of MXene is orders of magnitude higher than that of the other constitutes (polymer or interfaces), deformation and damage is expected within the weaker constitutes while MXene will experience only low strain and will remain in the elastic zone. Hence, an elastic-perfectly plastic constitutive model for MXene was used. The value of E was taken as 330 GPa, based on the above-mentioned experimental data [68]. Other material parameters included Poisson's ratio  $\nu=0.23$ , density  $(\rho)=3.2~gm/cm^3$ , and  $\sigma_y=20~{\rm GPa}~[61,73]$ , though density values will have minimum impact in static and quasi-static simulations.

# 2.3. Contact interaction model

The contact interaction properties are critical to capture film response. As indicated in Fig. 2, two types of contact are present in the model, namely the MXene-MXene and the MXene-polymer interactions. The MXene-MXene interaction depends on processing and can include frictional interaction due to uneven adjacent surfaces, a glue-like response due to surface functionalization, atomic bond level interactions, or a combination of these [27,34,35,46,47,58,68,74,75]. To capture this range of responses, a cohesive surface-based contact approach in which traction-separation constitutive law was used to model initial contact response, damage initiation, and failure of cohesive bonds as implemented in ABAQUS [76].

Fig. 3a shows the cohesive model, where the peak  $t_i^{max}$  represents the point of damage initiation or bond strength, and the line post peak represents damage evolution or softening response post failure. The softening response can be defined by the shaded area under the curve (energy release rate  $G_{TC}$ ) or separation for debonding ( $\delta_i^f$ ). The slope initial stiffness is taken from computational consideration since multiple



Type of interaction	Strength (MPa)	Energy release rate (G <sub>c</sub> in /Jm²)	
Electrostatic	64	0.2	
Hydrogen	55	0.15	
Van-der Walls	20	0.02	
Viscous shear	12.9	0.008	

**Fig. 3.** Constitutive material models for contact interactions (a) cohesive contact model showing isotropic traction-separation criteria for damage initiation and evolution, where i represents the three cartesian directions and (b) related strength and energy release rate for different types of contact interactions taken from literature [31,77,78]. The shear traction at failure or  $t_n^{max}$  and energy area under the curve or  $G_{TC}$  corresponds to the type of interaction assumed for contact while the initial slope  $K_i$  or  $K_i'$  is taken from computational consideration.

(b)

values (indicated by  $K_i$  or  $K_i'$ ) can be used with the same values of triangle peak ( $t_i^{max}$ ) and triangle base ( $\delta_i^f$ ), leading to the same area ( $G_{TC}$ ). Here, maximum shear strength criteria was used for damage initiation as represented by equation (1), where the damage initiates when the contact shear stress reaches the corresponding maximum allowed shear stress for the bond. Post initiation, the damage evolution follows the energy release rate criteria for the chosen bond.

$$\left\{ \frac{\langle t_1 \rangle}{t_1^o}, \frac{t_2}{t_2^o}, \frac{t_3}{t_3^o} \right\} = 1$$
 equation 1

where  $t_1^o$ ,  $t_2^o$ , and  $t_3^o$  represents the maximum contact shear stress in the normal( $t_1^o$ ) and in-plane directions ( $t_2^o$  and  $t_3^o$ ),

Fig. 3b summarizes bond strength and energy release rates for different types of potential bonds that can be present in MPC [31,77,78]. Two sets of bond properties, namely electrostatic and viscous shear response, were considered to represent strong and weak interactions, respectively. The strong electrostatic interaction used  $t_i^0 = 64$  MPa and  $G_{TC} = 0.2 \ J/m^2$ . The weak viscous interaction used  $t_i^0 = 12.9$  MPa and  $G_{TC} = 0.008 \ J/m^2$ . While damage initiation and damage evolution criteria depend on the selected bond, the slope  $K_i$  can take multiple values for the same selected  $t_i^0$  and  $G_{TC}$ , as explained earlier. Here,  $K_i = 1000$  GPa was used for computational stability consideration.

Post cohesive bond breakage, surfaces could slide past one under frictional contact. A hard contact model was used in the normal direction and isotropic columbic frictional interaction in the tangential direction [79–81]. The hard contact is described by equation (2), where contact pressure ( $P_c$ ) is active when the gap (h) between the two surfaces reduces to zero, i.e., h < 0. The isotropic columbic frictional interaction relates equivalent tangential stress ( $\tau_{eq}$ ) to  $P_c$  via frictional coefficient ( $\mu$ ) describing the surface roughness, as described in equation 3. Coefficient  $\mu = 0.1$  was used to represent a comparatively smoother surface.

$$P_c = 0$$
 for  $h < 0$  (open contact) equation 2

 $P_c > 0$  for h = 0 (closed contact)

 $au_{eq} < \mu P_c$  for "no slip" condition equation 3  $au_{eq} = \mu P_c$  for "slip" where  $au_{eq} = \sqrt{ au_1^2 + au_2^2}$ ,  $au_1$ ,  $au_2$  being the in-plane contact shears.

### 2.4. Meshing and simulation Strategy

The model was subjected to tensile load though displacement boundary conditions applied at both vertical ends. To model many complex contact interactions efficiently, ABAQUS/Explicit was employed whereby the governing dynamic equilibrium equation is solved explicitly through time using a central difference scheme. However, the solution is conditionally stable depending on time steps and element size. A slower loading achieved via shorter time steps and

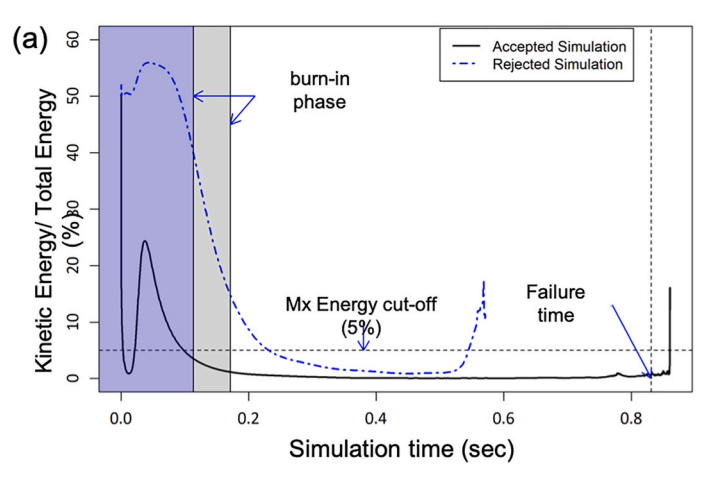
longer time duration can lead to quasi-static loading as required for the type of simulation under consideration. However, the solution may become inefficient in terms of time and computational resources required. Hence, alternative strategies of mass scaling to increase the minimum stable time increment [82,83] were used here to improve solution efficiency. Furthermore, to maintain uniform quasi-static conditions in the model with large AR for geometries, it is crucial to ensure that the mass-scaled models have sufficient stress waves traversing the entire model length. Hence, the mass scaling was adjusted to target analysis time consistent with at least 50 stress waves traversing the length of the model and by maintaining a ratio of kinetic energies (ALLKE) to total energies (ALLIE) to be <5 % for simulation prediction to be considered. The energy criteria were applied after the initial unstable or "burn-in" analysis stage, defined as 20 % of the simulation crash time. Values are only reported from the analysis that satisfied the above quasi-static loading conditions.

Fig. 4a shows examples of acceptable and rejected analyses based on the criteria outlined above, where the accepted simulations were below the 5 % kinetic energy ratio. For each accepted simulation, multiple elastic-plastic parameters were extracted from its stress-strain curve, as shown in a representative curve of Fig. 4b. The predicted parameters include elastic modulus (E) from the initial slope, ultimate tensile strength ( $\sigma_{UTS}$ ) from the peak of the curve, failure strength ( $\sigma_{ES}$ ) from the point of failure, and tensile toughness from the area under the curve ( $U_T$ ).

The model geometry was meshed using 4-noded two-dimensional elements with reduced integration (CPE4R), which provides a good balance between accuracy and efficiency with lower mesh sensitivity [84]. A global element size of 0.4 nm was chosen to mesh the geometry resulting in around 173000 elements, though the exact number varied from analysis to analysis due to randomness of geometry design (see S1). As discussed, mesh size is tied to analysis stability in dynamics explicit solution scheme, where finer mesh can slow the simulation or result in unstable analysis. Fig. 5 shows the results of mesh convergence studies performed for global element size of 0.8 nm–0.25 nm. The results were consistent across the multiple mesh sizes selected. The chosen global element size of 0.4 nm provided efficient results without compromising solution stability and time (see Fig. 5).

### 3. Results

Analysis was performed for three different MXene flake AR of 40, 60, and 75 with flake concentrations between 75 and 95 %, as detailed earlier. Fig. 6 shows the overall structural stress-strain response with increasing volume concentrations from left to right from all analyses. The outcome for strong interaction cases is shown in Fig. 6a and for weak interaction cases in Fig. 6b. A visual examination of the plot provides a quick view of how cohesive properties, concentration, and AR affect mechanical response. Clearly cohesive strength and concentration appears as an important factor impacting several facets of mechanical



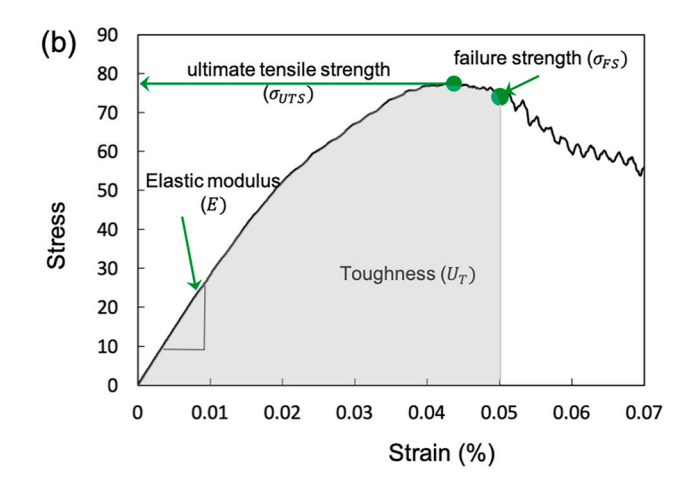


Fig. 4. Representative plots for (a) kinetic energy to total energy as a function of analysis time showing accepted vs rejected solutions and (b) stress-strain response for the structure with mechanical properties extracted from each curve. As indicated, the accepted simulation has kinetic energies below 5 % cut-off post the initial "burn-in" phase. The mechanical response of the MPC structure was extracted from the stress-strain response and included young modulus E from the initial slope, ultimate tensile strength  $\sigma_{UTS}$  from the peak of the curve, failure strength  $\sigma_{FS}$ , and tensile toughness  $U_T$  from the area under the curve shown as a shaded zone.

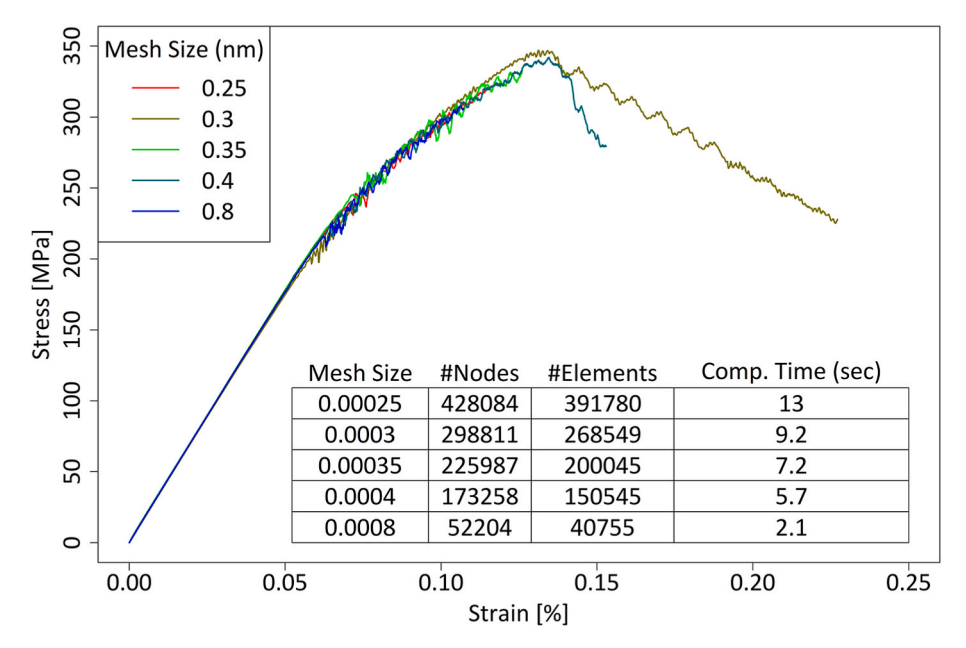


Fig. 5. Mesh convergence outcome with the table showing mesh details and plot with corresponding stress-strain response for the different global element sizes. The results across the different sizes were close, and the size of 0.4 nm was selected due to a balance of solution accuracy and efficiency.

response. However, larger variability in response such as for a given concentration or cohesive strength indicates that a combination of geometrical factors together with differences in localized microstructures resulting from the randomness in model generation can also have a significant impact on the outcome. Such detailed insights from these plots and the underlying mechanisms are discussed in the section that follows using the extracted elastoplastic values ( $\sigma_{UTS}$ ,  $U_T$ , and E) of Figs. 7–9. All values used for these plots are provided as supplementary information (SI-Tables 2 to 7).

# 3.1. Effect of cohesive strength

The cohesive contact interaction significantly impacts structural strength and toughness across all AR and flake concentrations, as visible in Figs. 7 and 8 and the table provided in SI. For example, for *fAR* of 75, the average  $\sigma_{UTS}$  for stronger interactions was 347  $\pm$  161 *MPa* compared to 115  $\pm$  39 *MPa* for the weaker interaction, marking a 3X increase. A similar 2X increase in strain-to-failure values was also measured from an

average of 12.6 % for stronger interaction from 6.2 % for the weaker interaction case. Correspondingly, a higher impact was felt in toughness (Fig. 8) with the 6X increase, with 291  $\pm$  226  $KJ/m^3$  for stronger interaction compared to  $50 \pm 24 \ KJ/m^3$  for the weaker case, though a larger scatter in values for the stronger interaction indicates potential influence of other factors on the outcome such as geometry variability and localized features (discussed later). This strong effect of cohesive interaction strength was consistent across all AR, with corresponding increases in  $\sigma_{UTS}$  for the strong interaction case being 3.5X and 3.1X for fAR of 60 and 40. The underlying mechanisms for the high influences of cohesive strength on strength and toughness can be attributed to delayed interlayer slippage, which is explained in Section 3.3.

In contrast to strength and toughness changes, the values for E were not significantly impacted by the changes in the contact interaction strength (Fig. 9). This is expected since E is extracted from small strain response of the structure where interface sliding or failure does not occur. Across all cases, the elastic modulus varied from a minimum of 207 GPa to 539.5 GPa. The E values for stronger interactions were 277  $\pm$ 

A. Prasad et al. Composites Part B 284 (2024) 111689

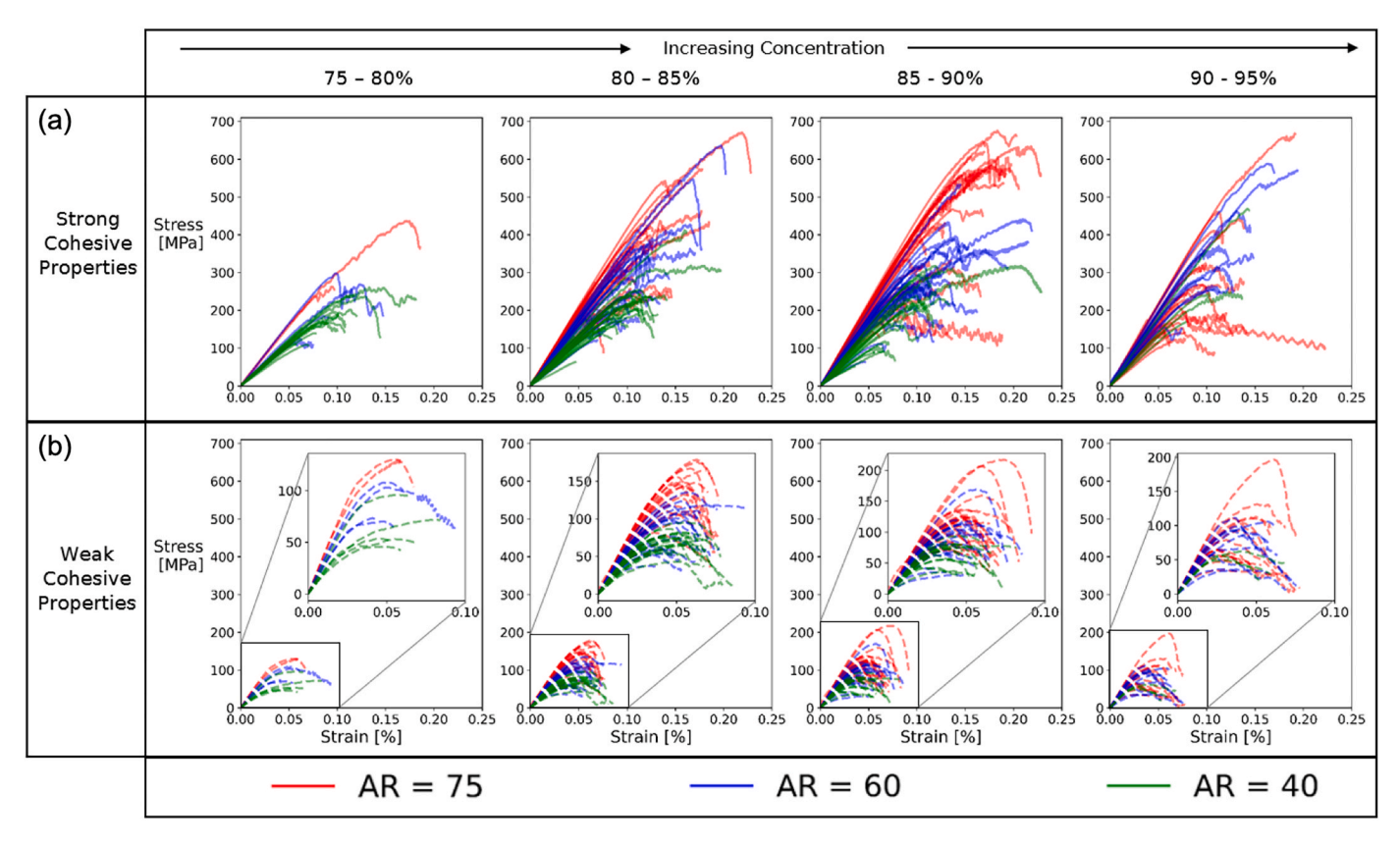


Fig. 6. Structural stress-strain response for the whole set of analysis showing the response of strong (top panel) vs. weak (bottom panel) cohesive properties and with increasing volume concentrations (left to right) for MXene flake aspect ratios of 40, 60, and 75. Contact strength has the most significant impact on strength and toughness.

 $36, 343 \pm 54$  *GPa*, and  $381 \pm 46$  *GPa*, respectively, for  $f_{AR}$  of 40, 60, and 75. The corresponding values for weaker interactions were  $307 \pm 52$  *GPa*,  $359 \pm 45$  *GPa*, and  $410 \pm 43$  *GPa*. Overall, stronger contact strength contact resulted in slightly reduced *E* (approximately 0.9X of their weak counterpart), but no significant influence was observed, as mentioned earlier.

### 3.2. Effect of flake concentration and AR

For high cohesive strength, the plots show a large spread in values of  $\sigma_{UTS}$  for all AR (Fig. 7a) indicating its weak relationship with concentration and influence of local structural features such as flake-polymer distribution or MXene overlap lengths which varies from model to model with the same flake concentration and AR due to randomness of model creation. Based on the trend lines marked,  $\sigma_{UTS}$  shows a slightly increasing trend with concentration for lower AR of 40 and 60 and a decreasing trend for AR of 75, though these relationships are weak as indicated by the trend line R-squared value. The toughness values (Fig. 8a) have a similar high scatter. For low cohesive strength, the plots (Fig. 7b) show a smaller scatter in  $\sigma_{UTS}$ , though weakly correlated with concentration, based on the trend line and their R-squared value. Furthermore, the strength is relatively stable with changing AR and concentration, except for AR of 75, which shows a decreasing trend with an increase in concentration. The values of E also showed scatter in values, with an overall increasing trend with concentration for all cases except for AR of 75 for strong contact interaction, where it remained flat (Fig. 9).

From these, a key conclusion can be drawn that though a weak correlation is found in elastoplastic response with AR, it is clear that a critical AR exists (here 75) above which the strength and toughness gets negatively impacted with increasing concentrations and elastic stiffness. This effect resonates with natural mineralized systems where increasing

AR leads to lower toughness [14,26]. Another key outcome of low correlation in elastoplastic response with global geometrical values, together with high dependence on cohesive strength, is that local structural features are expected to have a more substantial influence on response and failure. These aspects are explored in Section 3.3.

# 3.3. Damage and failure mechanism

The observed weak correlation of strength and toughness on concentration and a reversal of such correlation at higher AR point to a more substantial influence of two features, namely (1) local structural features such as flake distribution and interphase polymer zones and (2) interactions between MXene-MXene and MXene-polymer interface. To probe these structural influences on the failure mechanism, failure progression was examined in the structure from failure initiation up to failure time ( $t_f$ ). The model with maximum  $\sigma_{UTS}$  was selected for this, which was observed to occur for strong cohesion, with AR of 75 and fC range between 80 and 85 % (see Fig. 6). The failure mechanism was compared with its corresponding (i.e., strong interaction case with the same AR and fC range) minimum  $\sigma_{UTS}$  model. These responses are shown in Figs. 10 and 11.

Under uniaxial tension load, while MXene and polymer will primarily experience tension, contact interfaces can fail by shear or tension, depending on the location of the interface with respect to the loading direction. Furthermore, since MXene has significantly higher stiffness and strength than polymer or the interfaces, the polymer and the interfaces are expected to be the weakest points in the structure where failure will initiate, while MXene will experience under low strain.

Fig. 10 shows a close-up of the structure at failure with lines x-y or x'-y' drawn on top to indicate how failure propagates through the structure for the two selected extreme cases (for minimum and maximum  $\sigma_{UTS}$  with the same global geometrical parameters). For maximum ultimate

Composites Part B 284 (2024) 111689

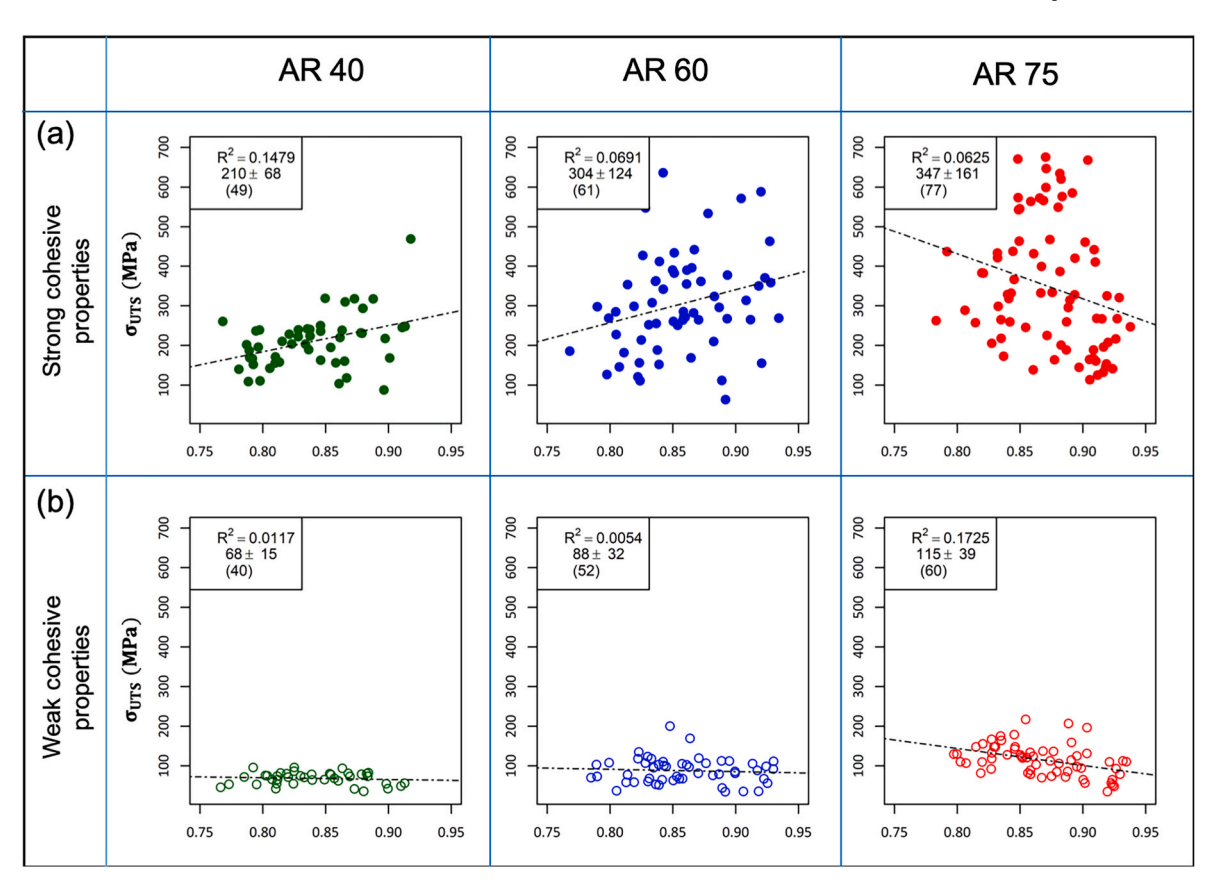


Fig. 7. Scatter plots for ultimate tensile strength  $\sigma_{UTS}$  in MPa extracted from the stress-strain response. Each plot also shows the average and standard deviation values in MPa, with the value in the bracket showing the total number of data points for each. The cohesive strength significantly alters the strength response, as reflected in the higher values of  $\sigma_{UTS}$ .

strength (Fig. 9a), structural failure occurs at two locations marked as "1" and "2". In both cases, the failure is initiated at the top exposed polymer layer marked as "x". At location "1", the failure propagates along small overlapping MXene-MXene interfaces and MXene-polymer contact until the crack gets arrested by MXene flakes, marked as "y". For location "2", two failures seem to originate marked by x-y and x'-y'. In both cases, failure initiates at the MXene-polymer interface and propagates through the polymer, finally getting arrested due to the presence of the MXene flake, as in the earlier location. For the case of minimum ultimate strength with similar global geometrical parameters (Fig. 9b), in the absence of a long MXene flake to arrest crack growth, the crack propagates through the interfaces and polymer to result in catastrophic failure of the film from both top and bottom.

Fig. 11 shows crack propagation using von-Mises plot at different time points post-failure initiation. The end of failure is marked by time  $t_f$ . For the maximum ultimate strength case location "2" is used for the plot. The yield strength of the polymer matrix is 31.5 MPa. Hence, to highlight the stress concentration points within the polymer, the vonmisses stress plot maximum is kept the same at 31.5 MPa for both cases. For the cases shown, the first failure initiation point is at the MXene-polymer interface at the top layer, indicated by the arrow. Once a crack is created, its propagation or arrest primarily depends on the local structural features. Structural features such as connected polymer layers or smaller interfaces lead to a fast propagation of cracks, while long MXene flakes in their path can lead to crack arrest. Here, for the high  $\sigma_{UTS}$  case, the presence of MXene flakes in the crack path led to the crack arrest from further penetrating for both the first and second failure initiation points, resulting in higher strength and toughness. In contrast, the absence of an MXene arresting layer and the presence of small overlapping flake lengths between adjacent layers allows for an easy failure path up after the failure initiates, resulting in a catastrophic

failure. The above mechanism is present for strong and weak interface cases, though the stiffness and strength are lower for weaker contact. Although the cases shown above are all initiated from a single side, failure can also be initiated on both sides, leading to double-sided catastrophic failures. This analysis also highlights the observation that MXene localized agglomeration can often lead to polymeric-rich regions, which in turn acts as a bottleneck for crack growth and catastrophic failure of thin films.

From the above, it can be concluded that while global features such as increasing MXene concentration or AR are essential in increasing structural stiffness, as seen in the increasing trend in elastic modulus (Fig. 9), it may come at the cost of strength and toughness as demonstrated above and in trend line plots at AR = 75. This is because local micromechanics features such as flake distribution, small overlapping lengths, and connected adjacent polymer layers become critical determining factors for damage initiation and propagation, leading to lower strength and toughness. The failure mechanism propagating along the weak interface in a nacre-like design is expected in materials with a higher AR of the mineral phase [60]. Correspondingly, the presence of MXene flake in the path of the crack leads to crack arrest and higher strength and toughness, as demonstrated in Fig. 10.

### 4. Summary and discussion

The paper uses parametrized FEA techniques to examine the mechanical response of layered MPC organized with a nacre-inspired brick-and-mortar architecture where MXene is the stiff brick, and PVA is the interphase polymer. The research aims to provide the overall response of such structures, identify critical geometrical features that lead to their response and failure, and offer guidelines for processing highly concentrated MXene thin films. This, in turn, required the generation of

Composites Part B 284 (2024) 111689

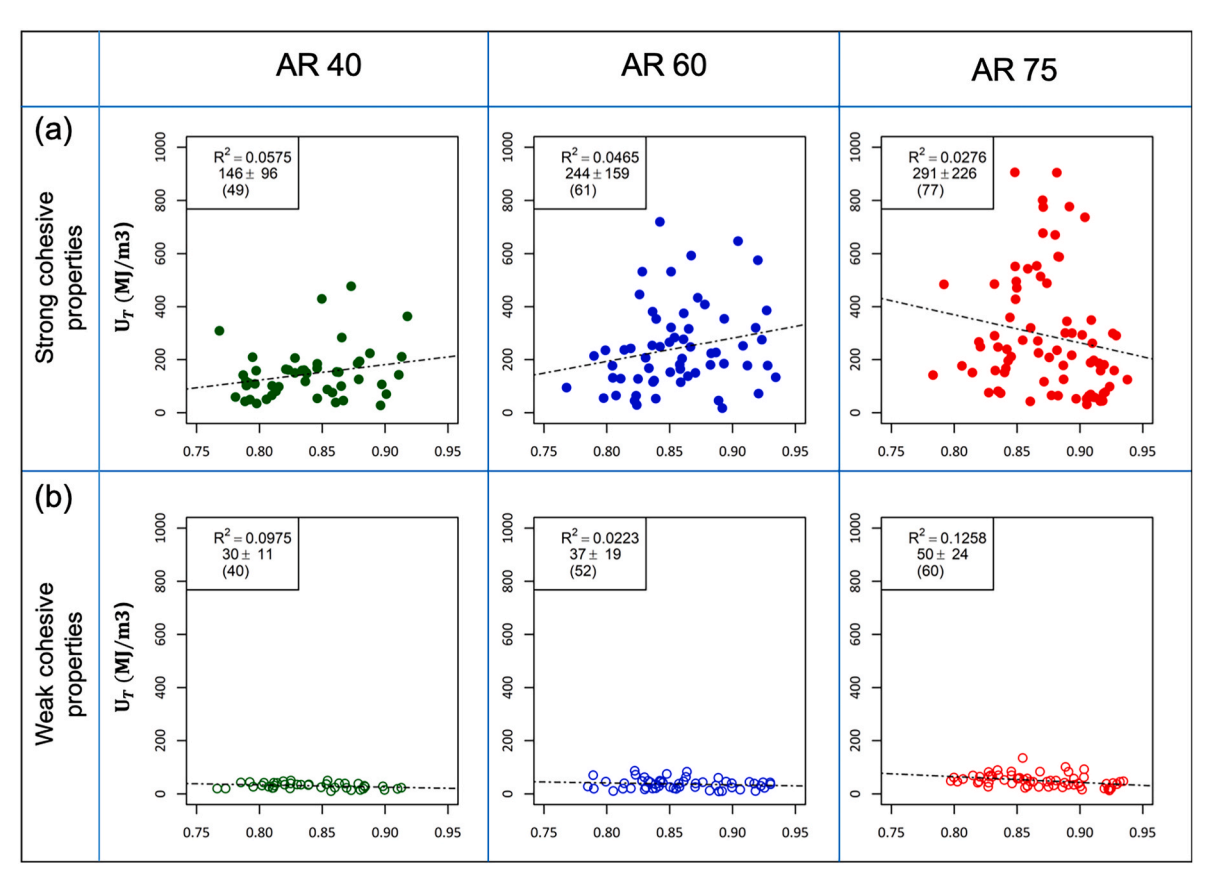


Fig. 8. Scatter plots for toughness  $U_T$  in  $MJ/m^3$  extracted from the stress-strain response. Each plot also shows the average and standard deviation values in  $KJ/m^3$ , with the value in the bracket showing the total number of data points for each. The cohesive strength significantly alters the toughness response, as reflected in the measure of E.

a large number of model geometries with random microstructure distribution such as that expected in real-world processing. To achieve the above goal, an automated model generation and post-processing framework was developed and presented in the paper. The interface interaction is another key determining feature of the model. Here, a surface-based cohesive contact was used for debonding and frictional contact for interaction after cohesive contact breakage. The contact strengths were selected corresponding to strong electrostatic interaction and weak viscous shear to represent the range of interface strengths in the MPC.

The investigation revealed that the values for E had an increasing trend with increasing concentration of MXene but no significant influence on cohesive strength or AR (Fig. 9). The above response is expected since E is extracted at small strains, at which time stiff MXene has a higher influence than interface interactions. Cohesive contact strength on the other hand significantly influenced the strength and toughness values (Figs. 7 and 8). Another key outcome of the study was the strong influence of microstructural features on strength and toughness (Figs. 10 and 11). Overall, across all simulations, the average and variance in E,  $\sigma_{UTS}$ , and  $U_T$  were calculated to be  $377 \pm 151$  GPa,  $250 \pm 176$  MPa, and  $193 \pm 200$   $KJ/m^3$  which captures the range of values predicted and also the large scatter in values across different structures.

As an analysis of the underlying reason for data scatter and the mechanism governing the response, two simulations with the same global geometrical parameters and interface strengths but with contrasting outcomes on strength and toughness were examined (Figs. 10 and 11). The above demonstrated the strong influence of microstructural features such as flake distribution, flake arrangement, and interphase polymer location features. For example, the presence of polymer features such as small overlapping lengths or interconnected polymers in adjacent layers can cause catastrophic failure, while the presence of a

large aspect ratio MXene flake in the path of a crack can arrest cracks. The subsection below further compares the results from this work against existing theoretical, computational, and experimental outcomes and evaluates the prediction sensitivity in presence of random defects.

# 4.1. Comparison with theoretical models

The above-observed outcomes of mechanical performance were evaluated in the context of existing theoretical frameworks of damage and failure in layered composites. Several models exist to predict responses for general composites, such as the rule-of-mixtures [85,86], the strength-based shear-lag model (SLM) model [86–89], and the energy-based cohesive-zone model (CZM) [86,90]. The rule-of-mixtures is the simplest of these models where the composite stiffness ( $E_{com}$ ) is the weighted average of its constituent property ( $E_i$ ) weighted by its volume concentrations ( $V_i$ ), i.e.,  $E_{com} = \sum_{i=1}^n V_i * E_i$ . Using the above,  $E_{com}$  for MPC is predicted to linearly increase from 231 to 313 GPa with a 70 %–95 % increase in MXene. The underlying assumptions of linear elastic response, equal strain distribution among its constituents, no slippage at interfaces, and no consideration of geometrical features such as AR makes the model have limited applicability for the composite considered here.

Other specialized models capturing the staggered pattern of reinforcement, AR and high volume concentration of stiffening components have been used to explain the strength and toughening mechanism of biocomposites [91–93]. Specifically, by including the influence of staggered mineral crystal but without slippage of interfaces, the elastic modulus is predicted by equation (4) below [91,92]. Using this model, the  $E_{com}$  calculated for the current set of materials and geometry ( $V_{\emptyset} = 95$  %, and  $AR_{\emptyset} = 40$ , 60, 75) varies from 275 GPa to 301 GPa with increasing AR s. These are in the range of simulation outcomes of E

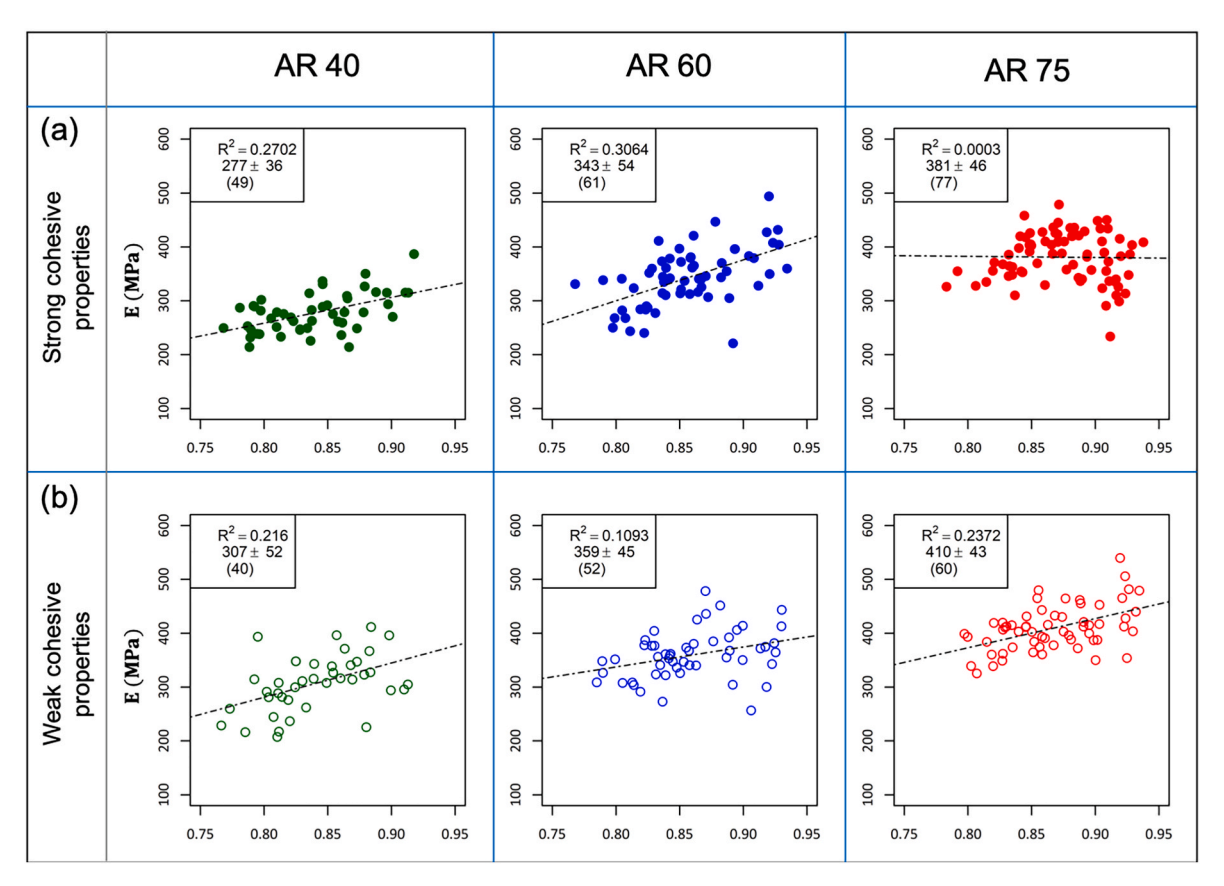


**Fig. 9.** Scatter plots for Young's modulus *E* in *MPa* extracted from the stress-strain response. Each plot also shows the average and standard deviation values in *GPa*, with the value in the bracket showing the total number of data points for each. The cohesive strength does not significantly alter the response at small strains, as reflected in the measure of *E*.

reported here.

$$\frac{1}{E_{com}} = \frac{4(1-V_{\varnothing})}{G_m V_{\varnothing}^2 A R_{\varnothing}^2} + \frac{1}{V_m * E_m}$$
 equation 4

 $V_{\varnothing}=$  volume concentration of mineral,  $G_m=$  shear modulus of matrix,  $AR_{\varnothing}=AR$  of mineral, and  $E_{\varnothing}, E_m$ , and  $E_{com}$  are Young's modulus of the mineral, matrix, and composites, respectively.

Since interface design is critical for composite performance, it is essential to analyze the outcomes in the context of models that incorporate interface response such as the SLM and CZM [86–90] and their modifications [26,93]. The basic SLM is shown in Fig. 12a, with equation 5a and b representing the shear  $(\tau_i)$  and tensile stress  $(\sigma_f)$  predictions along the fiber-matrix surface. The basic CZM shown in Fig. 12b is rooted in fracture mechanics and predicts energy for debonding  $(G_{CD})$  and pull out  $(G_{CP})$  under the fiber pullout test, given by equation (6). SLM predicts shear stress to be maximum at the fiber ends where the tensile stress is zero, i.e., no tensile stress transferred to the matrix at the fiber ends, which clearly is a limitation for the current analysis, as depicted via failure mode (Fig. 11) and stress plot (Fig. 12).

Given the geometry of the layered composite used and the differences in material and interface properties expected in MPC, the CZM is better equipped to predict debonding and crack growth for staggered brick-mortar design. Such is the case observed in the failure mechanism, where strain concentration at the polymer-MXene interface leads to failure initiation by localized debonding of the weak interfaces, finally resulting in gradual or rapid crack propagation depending on localized structural features. Hence, the energy-based fracture approach for interphase debonding, tensile and shear stress transfer at the filler ends, and frictional interaction post-debonding are together needed to capture the deformation modes of the brick-and-mortar organization with rough or wavy surfaces in contact.

$$\tau_i = \frac{E_f n \varepsilon_1}{2} \sinh\left(\frac{nx}{r}\right) \operatorname{sech}(n * s)$$
 equation 5a

$$\sigma_f = E_f \varepsilon_1 \{1 - \cosh\left(\frac{nx}{r}\right) \operatorname{sech}(n * s)\}$$
 equation 5b

$$G_{CD} = V_f s G_{IC}$$
 equation 6

where 
$$n=\sqrt{rac{E_m}{E_f(1+
u_m)l\left(rac{R}{r}
ight)}};$$
  $arepsilon_i=$  far-field axial strain,  $R=$  matrix radius,  $r=$ 

fiber radius, 2L =total fiber length,  $x=\pm L$ .  $E_m$  and  $E_f$  are Young's modulus of the matrix and the fiber,  $v_m=$  Poisson's ratio of the matrix, and  $s=\frac{L}{r}$  or AR of the fiber.  $G_{CD}=$  total work of debonding,  $G_{IC}=$  fracture energy of interface,  $V_f$  is the volume fraction of fiber, s, and L, and r as described earlier.

# 4.2. Comparison with computational results

The outcomes of the current study were also examined in the context of computational FEA work on MXene-based composites [35,40–44]. In one of these earlier works PMC (MXene-PVA and MXene-epoxy) nanocomposite with the random and aligned distribution of MXene flakes were examined using the representative volume element (RVE) technique [40]. The MXene volume fraction was 40 % or lower, and the average AR attained was 25–31. An interfacial layer of 5 nm with elastic stiffness at a factor of strength (0.25–1) of that of the polymer was incorporated. There are significant differences in the study approach compared to the current work, such as inverse analysis to tweak material properties to match experiments, low volume concentration, and significantly stronger interphases than the values used in the current

A. Prasad et al.

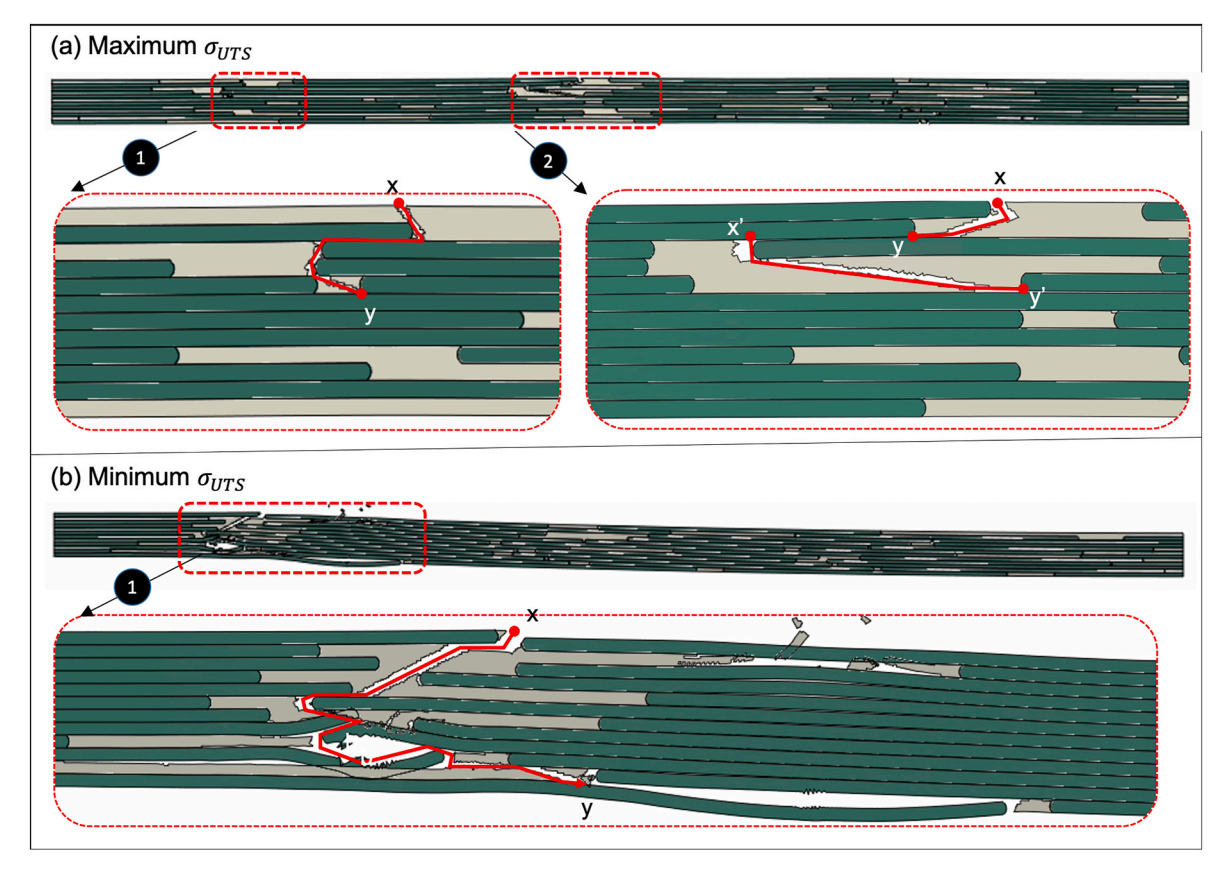


**Fig. 10.** Figure illustrating the failure state for the two cases with the same global geometrical parameters (AR of 75 and fC between 80 % and 85 %) and strong cohesive strength, but with maximum and minimum  $\sigma_{UTS}$  outcome. Lines x-y or x'-y' highlight failure paths. (a) The presence of long MXene flakes in the path of the crack leads to crack arrest, resulting in high strength and toughness. (b) The absence of arresting MXene flake and the presence of small overlapping flake lengths and interconnected polymer layers results in catastrophic failure.

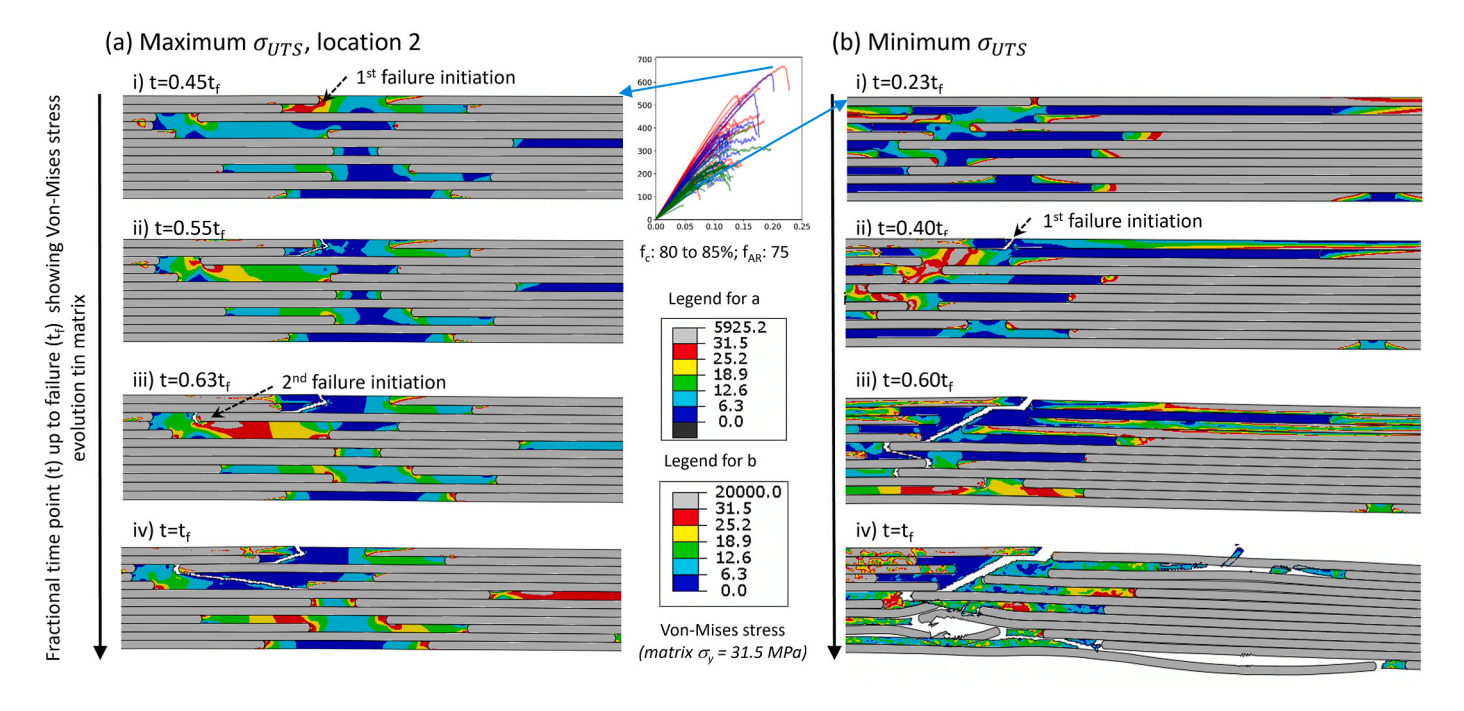


Fig. 11. Figure illustrating the mechanism of damage initiation and failure for the two cases of Fig. 10, with the same global geometrical parameters (AR of 75 and fC between 80 % and 85 %) and strong cohesive strength, as indicated by the stress-strain plot at the center. The images show Von-Mises stress evolution in matrix at different analysis time point (t) as a fraction of total time to failure ( $t_f = 1$ ). (a) Maximum  $\sigma_{UTS}$  case failure location "2" demonstrates gradual failure due to the presence of MXene flakes in the path of the crack. (b) Minimum  $\sigma_{UTS}$  case demonstrates catastrophic failure due to the presence of small overlapping flake lengths and interconnected polymer layers.

Fig. 12. Mechanics model for predicting debonding and failure of interface-matrix interactions, namely (a) the shear lag model or SLM and (b) the cohesive zone model or CZM. The CZM is an energy-based approach for evaluating interface failure and is rooted in fracture mechanics, where the mode of crack opening and propagation determines interface failure.

work. Hence, while a direct comparison of results is not possible, a few relevant outcomes included increased stiffness and strength with increasing concentration, AR, and alignment of MXene flakes, as observed from the current work for the lower range of concentration and AR. A related work examined similar architecture with RVE approach but much lower reinforcement of carbon and MXene filled nanocomposites (maximum 6.4 vol% MXene) randomly placed in epoxy and interface of comparable strength as the epoxy matrix [35,41]. Linear elastic properties were considered for all material, with interface layers perfectly bonded to the matrix. The above differences (low volume concentration, two different inclusion, interfaces stiffer than matrix and bonded, linear elasticity for polymers) all together makes the outcome not directly comparable with the current work, but the strong effect of microstructure on the mechanical outcomes (difference of aligned fiber vs random fiber distribution response) can be noted from this work.

In another FEA-based computational work on bioinspired MPC configuration used tied contact between MXene and polymer interfaces [44], thus assuming the perfect transfer of stresses with no possibility of failure of the interfaces, which is quite different from the current analysis. There were multiple other differences with the current model, such as using a lower concentration of MXene (40 wt%) and only considering elastic responses. The simulation also predicted increased *E* and strength with increasing MXene and increased stress transfer from polymer to MXene. However, the latter outcome came under the limitation of tied contact for interfaces.

Another recent study had an integrated experimental MPC processing with FEA to examine the influence of random low MXene reinforcement ( $<0.1\ vol\ \%$ ) on polyurethane matrix under tensile load [42]. The outcomes showed a 10 % difference between the simulations and experimental predictions. As compared with the mathematical model, the rules of mixtures showed the most significant difference from the experimental and simulation outcomes, with Halpin-Tsai and Hobbs model predicting comparable results. These outcomes were valid only for elastic responses since the analysis remained in elastic zone for all materials.

Finally, FEA study has also been performed on pure multi-layered MXene nanosheets under nanoindentation [39]. The analysis used tie-break contact of significantly high breaking strength between the MXene sheets than the cohesive interactions considered here. The results showed an increase in elastic modulus with increasing overlap between the adjacent sheets, highlighting the microstructure impact on the mechanical response.

Hence, none of the existing simulations modeled the high concentration of MXene or the presence of significantly weakened interfaces. The failure trends observed in our work come uniquely from these aspects of geometry and material properties, which are distinct from the earlier work but highly relevant in real-world systems. At the same time, commonality in outcome with the present work includes the trends in elastic modulus changes such as a function of AR or concentrations and the high influence of microstructure on the response be it by layer overlaps in pure sheets or the filler dispersion and layer direction in MPC. Furthermore, the earlier studies and their use of experimental data

for fitting or validation further support the integration of FEA with experimental work for such nanocomposites.

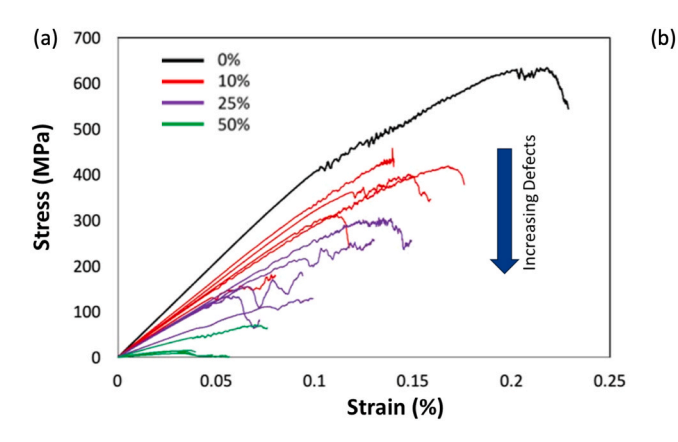
### 4.3. Comparison with experimental work on MPC

Finally, the deformation and failure outcomes of the result were compared against limited experimental studies of mechanical outcomes of MPC. An earlier study examined tensile stress-strain response for Ti<sub>3</sub>C<sub>2</sub>T<sub>r</sub>/PVA composite with variable weight % loading of MXene from 0 % (i.e., pure PVA) to 100 % (i.e., pure MXene) [61]. For the case of pure multilayered MXene film of 3.3 µm thickness, E was only reported to be 3.5 GPa, which is two orders of magnitude lower than typical values for pristine MXene sheets. While the study did not examine the underlying reason for stiffness reduction, it is expected that the lower strength can be attributed to the presence of structural defects, such as missing contact between MXene layers. This is further supported by the fact that the study reported an increase in tensile strength and failure strain with an increase in polymer concentration and noted that these indicate some stress was transferred between MXene and PVA. The above study clearly demonstrates the critical role of parameters such as film thickness and the quality of layer-to-layer contact, which affects interface strength and stress transfer between layers and their constituents on the outcome.

Another experimental work focused on the tensile and cyclic response of MXene films with film thickness varying from 2 to 17  $\mu m$  [94]. The mechanical properties of the film were reported to be inversely related to its thickness, E dropped from 17 GPa in 2.3  $\mu m$  thick film to 8 GPa in 17  $\mu m$  film. Similarly,  $\sigma_{UTS}$  dropped from 61 MPa to 36 MPa with film thickness. The strength outcomes dropping with increasing film thickness further supports that the result was also dominated by structural defects, highlighted in that paper.

Overall, these experimental results on MPC or layered pure MXene have shown much lower mechanical outcomes than reported in simulation studies, including the current work. However, there are few indicators to address the differences. The primary being one order of lower modulus for multi-layered MXene sheets compared to single layered sheets and the dependence of mechanical outcome on film thickness. These results suggest the role of defects and layering on the outcomes, which in turn are dependent on processing parameters. In comparison, the simulations had constant geometries with full contact and no defect.

To probe and validate the influence of defect on the mechanical response and connect closer with experimental data, additional simulations were performed to account for the presence and distribution of defects by turning off 10 %–50 % of the contacting surfaces to model broken bonds, keeping all other parameters the same. For each type of broken bond level, the distribution of broken bonds was randomly assigned to capture local structural influences. Fig. 13 shows the stress-strain response and property outcomes from one such set of simulations for AR of 75, strong cohesive contact, and fC of 80–85 %. The result clearly demonstrates the critical role of defects on mechanical outcomes with significant loss in E,  $\sigma_{UTS}$ , and  $U_S$  and strength with increasing bond defects from 0 % (defect free) to 50 %. Additionally, the influence of



	Defects			
	Elastic Modulus	Tensile Strength	Toughness	
	(GPa)	(MPa)	(KJ/m³)	
	Min - Max	Min – Max	Min - Max	
0% (1)	419	625	904	
10% (5)	316 – 363	182 - 420	80 – 430	
25% (5)	191 – 306	130 – 306	60 – 270	
50% (4)	140 - 237	9 – 71	0 - 30	

Fig. 13. (a) Structural stress-strain response with the addition of defect modeled as inactivated or broken bonds from 0 % to up to 50 % for AR of 75 and strong, cohesive interaction, and (b) corresponding elasto-plastic values. For each value of broken bonds, five different simulations were performed with a random distribution of MXene and broken bond location.

microstructure (i.e., broken bond distribution) was also observed in the five different stress-strain responses for the same percentage of broken bonds with but random broken bond distribution.

In summary in the context of experimental work, the current study while cannot provide a one-to-one match with the experiments due to variability in processing and layer attachments, it provides important guidelines for experimental work. For example, focusing on the fact that what drives failure with the same global parameters is localized microstructural features can guide experimentalist to selectively optimize processing parameters for flake distribution and overlap rather than solely on flake distribution. Similarly, the important influence and quantification of cohesive strength and broken bonds on the outcome can drive experimental focus towards compatible polymeric material choices for their uniform dispersion and interaction with MXene over pure strength perspective.

### 4.4. Broader implications and future directions

Overall, by presenting the structural stress-strain response and investigating underlying factors behind damage and failure mechanisms for layered MPC with high concentration including the presence and random distribution of broken bonds (mimicking defective interfaces), the current simulation captures important aspects beyond the influence of global geometry parameters on the MPC response. Highlighted below are broader implications and future directions for the work.

More often than not, efficiency in microstructure generation significantly enables to explore greater degree of parameter space to be modeled. The framework's automation and public availability of underlying scripts (see S1) will enable to extend the proposed framework beyond the current set of parameters and material combinations for structural integrity as well as for multi-physics modeling (such as combining structural integrity with thermal or electromagnetic performance) to cater the wide range of emerging applications for MPC. For example, the framework can be extended to analyze and guide design and processing of several layered MPC recently processed with different material combinations for their thermal and electrical conductivity, in addition to structural integrity [95-100]. The strong influence of microstructure on overall multi-functional performance compared to other factors provides guidance to experimentalists for such applications and beyond to focus on target design features with maximum influence on outcome. For example, the result indicates that experimental work towards optimizing processing parameters for greater dispersion of polymers to prevent their local agglomeration or forming interconnected layering will have the greatest influence on arresting crack. Similarly processing parameters to achieving greater overlap between stiff 2D sheets can be critical for improving strength outcomes as indicated in this work and by others [39].

Similarly, the framework can be utilized to analyze and quantify various microstructure design strategies for different 2D-filler systems and compare them with nacre-inspired geometries. For example, a recent work explored 2D boron nitride reinforcement in flake and spherical shapes for distribution and size optimization for strength and thermal conductivity enhancement in miniaturized power electronics application [101]. Such experimental work can greatly benefit from pre-assessment via simulations to better direct experimental resources. Similarly, the framework can be extended beyond layered design to provide capability to compare multiple design strategies. So future work can focus on extension of the automation framework to other shaped reinforcement. Several examples of such geometries in composites exist, few recent examples include spherical reinforcement such as spherical boron nitride particles [101] and bulk metallic glass composite structure [102] or dispersed MXene in coating for corrosion protection [103,104], but not limited to these applications or designs. Detailed simulation on these and other geometries can be performed as a pre-experiment assessment tool to efficiently compare different geometry and to better guide processing and performance assessment recourse.

Finally, the work such as this has multiple applications in multiscale simulations, for example, combining FEA models with MD outcomes. Specific to MPC and layered designs, the two simulation scales can be integrated to deduce interface energies for the targeted material combination of the MPC via MD simulations to capture the slippage and adhesion response which are otherwise difficult to capture through experiments [14]. Along the same lines, FEA simulations can be combined with various machine learning strategies for accelerated material design, prediction, and discovery as is increasingly becoming explored in materials science [105–108].

### 5. Conclusion

To conclude, a comprehensive study was performed to examine the mechanical response of MXene-polymer nanocomposites with bioinspired nacre-like architecture to offer valuable insights into their mechanics and guide the processing of such materials. The present study fills an important gap in the analysis of MPC with >70 % concentration of MXene. The results depict a combined influence of local geometrical features and stress transfer across the MXene and polymer materials and their weak interfaces to significantly alter predictions compared to theoretical models. Some of the key highlights from the work outcomes are listed below.

 While cohesive contact strength, flake concentration, and AR significantly affected composite strength and toughness, structural features, particularly flake distribution and overlapping lengths, emerged as dominant factors influencing crack initiation and

- propagation. Specifically, localized debonding reduces structural rigidity and delamination in multiple layers, impacting the overall strength and toughness.
- By contrasting the study findings with existing computational and experimental work, the research captures the unique aspects of MPC with high MXene concentrations and low cohesive interactions, emphasizing the importance of interfacial contact or lack thereof via the presence of defects. For example, experimental outcomes are predominantly governed by defects, which was also captured here by randomly including contact defects. This resulted in a transfer from a stiff composite response to orders of magnitude lower stiffness and strength with the same global parameters.
- The advantages of employing parameterized FEA with randomization of geometry allow us to capture the impact of complex geometries and boundary conditions on the deformation and failure mechanism, highlighting the suitability of this approach for modeling layered nanocomposites and as an pre-assessment tool to guide experimental resources.
- The framework can be extended beyond the current set of parameters and material combination through the availability of underlying automation scripts, thus expanding the future influence of the work.

The work thus provides insight into the performance of high-concentration MPC and the interplay between multiple parameters governing their performance. The work also attempts to stitch computational outcomes with theoretical models and experimental data to provide essential guidance for processing high-concentration MPC. Overall, the current work paves the way for the design and processing of improved MPC with enhanced mechanical outcomes to facilitate their incorporation in innovative applications across industries ranging from electronics to energy storage and sensing.

# CRediT authorship contribution statement

Anamika Prasad: Writing – review & editing, Writing – original draft, Visualization, Methodology, Investigation, Formal analysis, Conceptualization. Jason Hasse: Visualization, Software, Methodology, Formal analysis, Data curation. Timothy Steimle: Visualization, Methodology, Formal analysis, Data curation. Dhriti Nepal: Writing – review & editing, Methodology, Conceptualization. Geoffrey J. Frank: Writing – review & editing, Visualization, Formal analysis, Data curation. Vikas Varshney: Writing – review & editing, Visualization, Supervision, Resources, Project administration, Funding acquisition, Conceptualization.

# Declaration of competing interest

The authors declare that they have no known competing financial interests or personal relationships that could have appeared to influence the work reported in this paper.

### Data availability

Data will be made available on request.

# Acknowledgment

AP would like to thank Air Force Research Laboratory (AFRL) Materials and Manufacturing for the Summer Faculty Fellowship and also National Science Foundation (NSF) CAREER Grant # 2304788 for support on work on bioinspired designs. DP would like to acknowledge the Air Force Office of Scientific Research (AFOSR) grants (18RXCOR060 and 18RXCOR043). JH and TS would like to acknowledge internship support from AFRL through the Strategic Ohio Council for Higher Education (SOCHE). The work was possible through support from the DoD Supercomputing Resource Center (DSRC).

#### Appendix A. Supplementary data

Supplementary data to this article can be found online at https://doi.org/10.1016/j.compositesb.2024.111689.

#### References

- Oliveira FM, Gusmão R. Recent advances in the electromagnetic interference shielding of 2D materials beyond graphene. ACS Appl Electron Mater 2020;2: 3048–71. https://doi.org/10.1021/acsaelm.0c00545.
- [2] Gogotsi Y, Anasori B. The rise of MXenes. ACS Nano 2019;13:8491–4. https://doi.org/10.1021/acsnano.9b06394.
- [3] Naguib M, Kurtoglu M, Presser V, Lu J, Niu J, Heon M, Hultman L, Gogotsi Y, Barsoum MW. Two-dimensional nanocrystals produced by exfoliation of Ti3AlC2. Adv Mater 2011;23:4248–53.
- [4] VahidMohammadi A, Rosen J, Gogotsi Y. The world of two-dimensional carbides and nitrides (MXenes). Science 2021;372. https://doi.org/10.1126/science. abf1581
- [5] Sivasankarapillai VS, Sharma TSK, Hwa K-Y, Wabaidur SM, Angaiah S, Dhanusuraman R. MXene based sensing materials: current status and future perspectives. ES Energy Env 2022;15:4–14.
- [6] Gogotsi Y, Huang Q. MXenes: two-dimensional building blocks for future materials and devices. ACS Nano 2021;15:5775–80. https://doi.org/10.1021/ acsnano.1c03161.
- [7] Pan S, Yin J, Yu L, Zhang C, Zhu Y, Gao Y, Chen Y. 2D MXene-integrated 3D-printing scaffolds for augmented osteosarcoma phototherapy and accelerated tissue reconstruction. Adv Sci 2020;7:1901511.
- [8] Shahzad F, Alhabeb M, Hatter CB, Anasori B, Hong SM, Koo CM, Gogotsi Y. Electromagnetic interference shielding with 2D transition metal carbides (MXenes). Science 2016;353:1137–40.
- [9] Hunt G, Butler R, Budd C. Geometry and mechanics of layered structures and materials. Philos. Trans. R. Soc. Math. Phys. Eng. Sci. 2012;370:1723–9. https://doi.org/10.1098/rsta.2011.0539.
- [10] Riazi H, Nemani SK, Grady MC, Anasori B, Soroush M. Ti3C2 MXene–polymer nanocomposites and their applications. J Mater Chem A 2021;9:8051–98. https://doi.org/10.1039/D0TA08023C.
- [11] Jimmy J, Kandasubramanian B. MXene functionalized polymer composites: synthesis and applications. Eur Polym J 2020;122:109367.
- [12] Lian R, Ou M, Zhao Z, Gao Q, Liu X, Liu L, Chen X, Jiao C. Facile fabrication of novel fire-safe MXene@ IL-based epoxy nanocomposite coatings with enhanced thermal conductivity and mechanical properties. Prog Org Coating 2023;183: 107750
- [13] Lian R, Gao Q, Zhao Z, Ou M, Liu X, Liu L, Chen X, Jiao C. Hierarchical MXene@ PBA nanohybrids towards high-efficiency flame retardancy and smoke suppression of robust yet tough polymer nanocomposites at ultra-low additions. Composites Part B 2023;267:111074
- [14] Prasad A, Varshney V, Nepal D, Frank GJ. Bioinspired design rules from highly mineralized natural composites for two-dimensional composite design. Biomimetics 2023;8:500.
- [15] Wang J, Jiang D, Zhang Y, Du Y, Sun Y, Jiang M, Xu J, Liu J. High-strength nacre-like composite films based on pre-polymerised polydopamine and polyethyleneimine cross-linked MXene layers via multi-bonding interactions. J Colloid Interface Sci 2024;653:229–37. https://doi.org/10.1016/j.jcis.2023.09.074.
- [16] Han M, Shen W. Nacre-inspired cellulose nanofiber/MXene flexible composite film with mechanical robustness for humidity sensing. Carbohydr Polym 2022; 298:120109. https://doi.org/10.1016/j.carbpol.2022.120109.
- [17] Jiao E, Wu K, Liu Y, Lu M, Zhang H, Zheng H, Xu C, Shi J, Lu M. Robust bioinspired MXene-based flexible films with excellent thermal conductivity and photothermal properties. Composer Part Appl Sci Manuf 2021;143:106290. https://doi.org/10.1016/j.compositesa.2021.106290.
- [18] Jiao E, Wu K, Liu Y, Zhang H, Zheng H, Xu C, Shi J, Lu M. Nacre-like robust cellulose nanofibers/MXene films with high thermal conductivity and improved electrical insulation by nanodiamond. J Mater Sci 2022;57:2584–96.
- [19] Liu Z, Wang W, Tan J, Liu J, Zhu M, Zhu B, Zhang Q. Bioinspired ultra-thin polyurethane/MXene nacre-like nanocomposite films with synergistic mechanical properties for electromagnetic interference shielding. J Mater Chem C 2020;8:
- [20] Wang J, Ma X, Zhou J, Du F, Teng C. Bioinspired, high-strength, and flexible MXene/aramid fiber for electromagnetic interference shielding papers with joule heating performance. ACS Nano 2022;16:6700–11. https://doi.org/10.1021/ acsnano.2c01323.
- [21] Chen Q, Ma Z, Wang Z, Liu L, Zhu M, Lei W, Song P. Scalable, robust, low-cost, and highly thermally conductive anisotropic nanocomposite films for safe and efficient thermal management. Adv Funct Mater 2022;32:2110782.
- [22] Meyers MA, Lin AY-M, Chen P-Y, Muyco J. Mechanical strength of abalone nacre: role of the soft organic layer. J Mech Behav Biomed Mater 2008;1:76–85. https://doi.org/10.1016/j.jmbbm.2007.03.001.
- [23] Wang RZ, Suo Z, Evans AG, Yao N, Aksay IA. Deformation mechanisms in nacre. J Mater Res 2001;16:2485–93.
- [24] Lopez MI, Meza Martinez PE, Meyers MA. Organic interlamellar layers, mesolayers and mineral nanobridges: contribution to strength in abalone (Haliotis rufescence) nacre. Acta Biomater 2014;10:2056–64. https://doi.org/ 10.1016/j.actbio.2013.12.016.

- [25] Barthelat F, Yin Z, Buehler MJ. Structure and mechanics of interfaces in biological materials. Nat Rev Mater 2016;1:1–16.
- [26] Song J, Fan C, Ma H, Liang L, Wei Y. Crack deflection occurs by constrained microcracking in nacre. Acta Mech Sin 2018;34:143–50.
- [27] Verho T, Karesoja M, Das P, Martikainen L, Lund R, Alegría A, Walther A, Ikkala O. Hydration and dynamic state of nanoconfined polymer layers govern toughness in nacre-mimetic nanocomposites. Adv Mater 2013;25:5055–9.
- [28] Huang Z, Li X. Origin of flaw-tolerance in nacre. Sci Rep 2013;3:1693.
- [29] Li L, Ortiz C. Biological design for simultaneous optical transparency and mechanical robustness in the shell of placuna placenta. Adv Mater 2013;25: 2344–50. https://doi.org/10.1002/adma.201204589.
- [30] Vermeij GJ. Gastropod skeletal defences: land, freshwater, and sea compared. Vita Malacol 2015;13:1–25.
- [31] Luo Q, Nakade R, Dong X, Rong Q, Wang X. Effect of mineral-collagen interfacial behavior on the microdamage progression in bone using a probabilistic cohesive finite element model. J Mech Behav Biomed Mater 2011;4:943–52.
- [32] Ni H, Fan X, Zhou F, Guo G, Lee JY, Seeman NC, Kim D-N, Yao N, Chaikin PM, Han Y. Direct visualization of floppy two-dimensional DNA origami using cryogenic electron microscopy. iScience 2022;25.
- [33] Li R, Madhavacharyula A, Du Y, Adepu H, Choi JH. Mechanics of dynamic and deformable DNA nanostructures. Chem Sci 2023, 14, 8018-8046.
- [34] Wang Y, Ural A. Effect of modifications in mineralized collagen fibril and extrafibrillar matrix material properties on submicroscale mechanical behavior of cortical bone. J Mech Behav Biomed Mater 2018;82:18–26. https://doi.org/ 10.1016/j.jmbbm.2018.03.013.
- [35] Kilikevičius S, Kvietkaitė S, Mishnaevsky L, Omastová M, Aniskevich A, Zeleniakienė D. Novel hybrid polymer composites with graphene and MXene nano-reinforcements: computational analysis. Polymers 2021;13:1013.
- [36] Wei X, Kysar JW. Experimental validation of multiscale modeling of indentation of suspended circular graphene membranes. Int J Solid Struct 2012;49:3201–9.
- [37] Mortazavi B, Rabczuk T. Multiscale modeling of heat conduction in graphene laminates. Carbon 2015;85:1–7.
- [38] Chandra Y, Adhikari S, Flores ES. Advances in finite element modelling of graphene and associated nanostructures. Mater Sci Eng R Rep 2020;140:100544.
- [39] Zeleniakiene D, Monastyreckis G, Aniskevich A, Griskevicius P. Deformation and failure of MXene nanosheets. Materials 2020;13:1253. https://doi.org/10.3390/ ma13051253.
- [40] Monastyreckis G, Mishnaevsky Jr L, Hatter CB, Aniskevich A, Gogotsi Y, Zeleniakiene D. Micromechanical modeling of MXene-polymer composites. Carbon 2020;162:402–9.
- [41] Kilikevicius S, Kvietkaite S, Zukiene K, Omastova M, Aniskevich A, Zeleniakiene D. Numerical investigation of the mechanical properties of a novel hybrid polymer composite reinforced with graphene and MXene nanosheets. Comput Mater Sci 2020;174. https://doi.org/10.1016/j. commatsci.2019.109497.
- [42] Sanaka R, Sahu SK. FEM based RVE modeling for estimating axial modulus of polyurethane composite reinforced with MXene. Int. J. Interact. Des. Manuf. LUIDeM 2023:1–11
- [43] Rong C, Su T, Li Z, Chu T, Zhu M, Yan Y, Zhang B, Xuan F-Z. Elastic properties and tensile strength of 2D Ti3C2Tx MXene monolayers. Nat Commun 2024;15:1566.
- [44] Srivatsa S, Packo P, Mishnaevsky Jr L, Uhl T, Grabowski K. Deformation of bioinspired MXene-based polymer composites with brick and mortar structures: a computational analysis. Materials 2020;13:5189
- [45] Tushtev K, Murck M, Grathwohl G. On the nature of the stiffness of nacre. Mater Sci Eng C 2008;28:1164–72. https://doi.org/10.1016/j.msec.2007.10.039.
- [46] Barthelat F, Tang H, Zavattieri PD, Li C-M, Espinosa HD. On the mechanics of mother-of-pearl: a key feature in the material hierarchical structure. J Mech Phys Solid 2007;55:306–37. https://doi.org/10.1016/j.jmps.2006.07.007.
- [47] Rabiei R, Bekah S, Barthelat F. Failure mode transition in nacre and bone-like materials. Acta Biomater 2010;6:4081–9.
- [48] Levi-Kalisman Y, Falini G, Addadi L, Weiner S. Structure of the nacreous organic matrix of a bivalve mollusk shell examined in the hydrated state using cryo-TEM. J Struct Biol 2001;135:8–17. https://doi.org/10.1006/jsbi.2001.4372.
- [49] Ji B, Gao H. Mechanical properties of nanostructure of biological materials. J Mech Phys Solid 2004;52:1963–90. https://doi.org/10.1016/j. jmps.2004.03.006.
- [50] Wilbrink DV, Utz M, Ritchie RO, Begley MR. Scaling of strength and ductility in bioinspired brick and mortar composites. Appl Phys Lett 2010;97:193701.
- [51] Li Z-K, Wei Y, Gao X, Ding L, Lu Z, Deng J, Yang X, Caro J, Wang H. Antibiotics separation with MXene membranes based on regularly stacked high-aspect-ratio nanosheets. Angew Chem Int Ed 2020;59:9751–6.
- [52] Liu M, Zhuo Y, Sarycheva A, Gogotsi Y, Bissett MA, Young RJ, Kinloch IA. Deformation of and interfacial stress transfer in Ti3C2 MXene–polymer composites. ACS Appl Mater Interfaces 2022;14:10681–90.
- [53] Alhabeb M, Maleski K, Anasori B, Lelyukh P, Clark L, Sin S, Gogotsi Y. Guidelines for synthesis and processing of two-dimensional titanium carbide (Ti3C2T x MXene). Chem Mater 2017;29:7633–44.
- [54] Lipatov A, Alhabeb M, Lukatskaya MR, Boson A, Gogotsi Y, Sinitskii A. Effect of synthesis on quality, electronic properties and environmental stability of individual monolayer Ti3C2 MXene flakes. Adv. Electron. Mater. 2016;2: 1600255
- [55] Shekhirev M, Busa J, Shuck CE, Torres A, Bagheri S, Sinitskii A, Gogotsi Y. Ultralarge flakes of Ti3C2T x MXene via soft delamination. ACS Nano 2022;16: 13695–703.
- [56] Feng W, Luo H, Wang Y, Zeng S, Tan Y, Zhang H, Peng S. Ultrasonic assisted etching and delaminating of Ti3C2 Mxene. Ceram Int 2018;44:7084–7.

- [57] Chen L, Shi X, Yu N, Zhang X, Du X, Lin J. Measurement and analysis of thermal conductivity of Ti3C2Tx MXene films. Materials 2018;11:1701.
- [58] Cao W, Ma C, Tan S, Ma M, Wan P, Chen F. Ultrathin and flexible CNTs/MXene/cellulose nanofibrils composite paper for electromagnetic interference shielding. Nano-Micro Lett 2019;11:72. https://doi.org/10.1007/s40820-019-0304-y.
- [59] Zhou B, Zhang Z, Li Y, Han G, Feng Y, Wang B, Zhang D, Ma J, Liu C. Flexible, robust, and multifunctional electromagnetic interference shielding film with alternating cellulose nanofiber and MXene layers. ACS Appl Mater Interfaces 2020;12:4895–905. https://doi.org/10.1021/acsami.9b19768.
- [60] Jin X, Wang J, Dai L, Liu X, Li L, Yang Y, Cao Y, Wang W, Wu H, Guo S. Flame-retardant poly(vinyl alcohol)/MXene multilayered films with outstanding electromagnetic interference shielding and thermal conductive performances. Chem Eng J 2020;380:122475. https://doi.org/10.1016/j.cej.2019.122475.
- [61] Ling Z, Ren CE, Zhao M-Q, Yang J, Giammarco JM, Qiu J, Barsoum MW, Gogotsi Y. Flexible and conductive MXene films and nanocomposites with high capacitance. Proc Natl Acad Sci USA 2014;111:16676–81. https://doi.org/ 10.1073/pnas.1414215111.
- [62] Peresin MS, Habibi Y, Zoppe JO, Pawlak JJ, Rojas OJ. Nanofiber composites of polyvinyl alcohol and cellulose nanocrystals: manufacture and characterization. Biomacromolecules 2010;11:674–81.
- [63] Yeum JH, Ji BC, Noh SK, Jeon HY, Kwak JW, Lyoo WS. Effect of syndiotacticity on the morphology of water-soluble low molecular weight poly (vinyl alcohol) by solution copolymerization of vinyl pivalate/vinyl acetate in tetrahydrofuran and saponification. Polymer 2004;45:4037–43.
- [64] Yao Y, Jin S, Wang M, Gao F, Xu B, Lv X, Shu Q. MXene hybrid polyvinyl alcohol flexible composite films for electromagnetic interference shielding. Appl Surf Sci 2022;578:152007.
- [65] Liu R, Li W. High-thermal-stability and high-thermal-conductivity Ti3C2T x MXene/poly (vinyl alcohol)(PVA) composites. ACS Omega 2018;3:2609–17.
- [66] Pan Y, Fu L, Zhou Q, Wen Z, Lin C-T, Yu J, Wang W, Zhao H. Flammability, thermal stability and mechanical properties of polyvinyl alcohol nanocomposites reinforced with delaminated Ti3C2Tx (MXene). Polym Compos 2020;41:210–8.
- [67] Woo JH, Kim NH, Kim SI, Park O-K, Lee JH. Effects of the addition of boric acid on the physical properties of MXene/polyvinyl alcohol (PVA) nanocomposite. Composites Part B 2020;199:108205.
- [68] Lipatov A, Lu H, Alhabeb M, Anasori B, Gruverman A, Gogotsi Y, Sinitskii A. Elastic properties of 2D Ti3C2Tx MXene monolayers and bilayers. Sci Adv 2018;4: eaat0491.
- [69] Wei C, Wu C. Nonlinear fracture of two-dimensional transition metal carbides (MXenes). Eng Fract Mech 2020;230. https://doi.org/10.1016/j. engfracmech.2020.106978.
- [70] Borysiuk VN, Mochalin VN, Gogotsi Y. Molecular dynamic study of the mechanical properties of two-dimensional titanium carbides Tin+ 1Cn (MXenes). Nanotechnology 2015;26:265705.
- [71] Khaledialidusti R, Anasori B, Barnoush A. Temperature-dependent mechanical properties of Tin+1CnO2 (n = 1, 2) MXene monolayers: a first-principles study. Phys Chem Chem Phys 2020;22:3414–24. https://doi.org/10.1039/ C9CP06721C
- [72] Plummer G, Anasori B, Gogotsi Y, Tucker GJ. Nanoindentation of monolayer Tin + 1CnTx MXenes via atomistic simulations: the role of composition and defects on strength. Comput Mater Sci 2019;157:168–74.
- [73] Zhao T, Zhang S, Guo Y, Wang Q. TiC 2: a new two-dimensional sheet beyond MXenes. Nanoscale 2016;8:233–42.
- [74] Heckler JE, Neher GR, Mehmood F, Lioi DB, Pachter R, Vaia R, Kennedy WJ, Nepal D. Surface functionalization of Ti3C2T x MXene nanosheets with catechols: implication for colloidal processing. Langmuir 2021;37:5447–56.
- [75] Tian W, VahidMohammadi A, Wang Z, Ouyang L, Beidaghi M, Hamedi MM. Layer-by-layer self-assembly of pillared two-dimensional multilayers. Nat Commun 2019;10:2558.
- [76] Abaqus DS. ABAQUS documentation (6.14). 2014. Provid. RI.
- [77] Siegmund T, Allen MR, Burr DB. Failure of mineralized collagen fibrils: modeling the role of collagen cross-linking. J Biomech 2008;41:1427–35. https://doi.org/ 10.1016/j.jbiomech.2008.02.017.
- [78] Ji B. A study of the interface strength between protein and mineral in biological materials. J Biomech 2008;41:259–66. https://doi.org/10.1016/j. ibiomech.2007.09.022.
- [79] Oden JT, Martins J. Models and computational methods for dynamic friction phenomena. Comput Methods Appl Mech Eng 1985;52:527–634.
- [80] Wriggers P. Finite element algorithms for contact problems. Arch Comput Methods Eng 1995;2:1–49.
- [81] Wriggers P. Finite element methods for contact problems with friction. Tribol Int 1996;29:651–8.
- [82] Prior AM. Applications of implicit and explicit finite element techniques to metal forming. J Mater Process Technol 1994;45:649–56.
- [83] Hughes TJ. The finite element method: linear static and dynamic finite element analysisCourier Corporation. 2012.
- [84] Sun EQ. Shear locking and hourglassing in MSC Nastran, ABAQUS, and ANSYS. In: Msc softw. Users meet; 2006. p. 1–9.
- [85] Tsai S. Introduction to composite materials. Routledge; 2018.
- [86] Clyne TW, Hull D. An introduction to composite materials. Cambridge university press; 2019.
- [87] Fukuda H, Chou T-W. An advanced shear-lag model applicable to discontinuous fiber composites. J Compos Mater 1981;15:79–91.
- [88] Nardone VC, Prewo KM. On the strength of discontinuous silicon carbide reinforced aluminum composites. Scripta Metall 1986;20:43–8.

- [89] Cox HL. The elasticity and strength of paper and other fibrous materials. Br J Appl Phys 1952;3:72.
- [90] Ming-Yuan H, Hutchinson JW. Crack deflection at an interface between dissimilar elastic materials. Int J Solid Struct 1989;25:1053–67.
- [91] Jäger I, Fratzl P. Mineralized collagen fibrils: a mechanical model with a staggered arrangement of mineral particles. Biophys J 2000;79:1737–46.
- [92] Gao H, Ji B, Jäger IL, Arzt E, Fratzl P. Materials become insensitive to flaws at nanoscale: lessons from nature. Proc Natl Acad Sci USA 2003;100:5597–600.
- [93] Song ZQ, Ni Y, Peng LM, Liang HY, He LH. Interface failure modes explain non-monotonic size-dependent mechanical properties in bioinspired nanolaminates. Sci Rep 2016;6:1–9.
- [94] Luo S, Patole SP, Anwer S, Li B, Ogogotsi O, Zahorodna V, Balitskyi V, Liao K. Tensile behaviors of Ti3C2Tx (MXene) films. Nanotechnology 2020;31(39): 395704.
- [95] Malik R, Parida R, Parida BN, Nayak NC. Structural, thermal and dielectric properties of 2D layered Ti3C2Tx (MXene) filled poly (ethylene-co-methyl acrylate)(EMA) nanocomposites. J Appl Polym Sci 2023;140:e53460.
- [96] Lyu S, Chang H, Zhang L, Wang S, Li S, Lu Y, Li S. High specific surface area MXene/SWCNT/cellulose nanofiber aerogel film as an electrode for flexible supercapacitors. Composites Part B 2023;264:110888.
- [97] Kim J-B, Vu MC, Seo BK, Mani D, Anand S, Jeong T-H, Kim S-R. Multilayered graphene fluoride and Ti3C2Tx MXene-based aramid nanofiber films with excellent thermal conductivity and electromagnetic interference shielding performance. Colloids Surf A Physicochem Eng Asp 2024;685:133121.
- [98] Checko S, Ju Z, Zhang B, Zheng T, Takeuchi ES, Marschilok AG, Takeuchi KJ, Yu G. Fast-charging, binder-free lithium battery cathodes enabled via multidimensional conductive networks. Nano Lett 2024, 24(5): 1695-702.
- [99] Guo Z, Ren P, Yang F, Wu T, Zhang L, Chen Z, Ren F. Robust multifunctional composite films with alternating multilayered architecture for highly efficient

- electromagnetic interference shielding, Joule heating and infrared stealth. Composites Part B 2023;263:110863.
- [100] Yang B, Wang H, Zhang M, Jia F, Liu Y, Lu Z. Mechanically strong, flexible, and flame-retardant Ti3C2Tx MXene-coated aramid paper with superior electromagnetic interference shielding and electrical heating performance. Chem Eng J 2023;476:146834.
- [101] Yang S, Huang Z, Hu Q, Zhang Y, Wang F, Wang H, Shu Y. Proportional optimization model of multiscale spherical BN for enhancing thermal conductivity. ACS Appl Electron Mater 2022;4:4659–67.
- [102] Ding H, Gong P, Chen W, Peng Z, Bu H, Zhang M, Tang X, Jin J, Deng L, Xie G, Wang X, Yao K, Schroers J. Achieving strength-ductility synergy in metallic glasses via electric current-enhanced structural fluctuations. Int J Plast 2023;169: 103711. https://doi.org/10.1016/j.ijplas.2023.103711.
- [103] Zhao X, Fan B, Qiao N, Soomro RA, Zhang R, Xu B. Stabilized Ti3C2Tx-doped 3D vesicle polypyrrole coating for efficient protection toward copper in artificial seawater. Appl Surf Sci 2024;642:158639.
- [104] Li C, Liu Y, Yu Q, Sun S, Liu S, Zhao C, Wang X, Yang S, Yu B, Cai M. A composite coating based on Ti3C2Tx MXene and M16 corrosion inhibitor for self-healing anti-corrosion and wear resistance. Surf Coat Technol 2024;476:130281.
- [105] Ma J, Sun S. In silico optimization of actuation performance in dielectric elastomer composites via integrated finite element modeling and deep learning. Theor. Appl. Mech. Lett. 2024;14:100490.
- [106] Lew AJ, Jin K, Buehler MJ. Designing architected materials for mechanical compression via simulation, deep learning, and experimentation. npj Comput Mater 2023;9:80.
- [107] Yang Z, Buehler MJ. Fill in the blank: transferrable deep learning approaches to recover missing physical field information. Adv Mater 2023;35:2301449.
- [108] Lee J, Park D, Park K, Song H, Kim T-S, Ryu S. Optimization of grid composite configuration to maximize toughness using integrated hierarchical deep neural network and genetic algorithm. Mater Des 2024;238:112700.